ULTRAFAST LASER-MATERIAL PROCESSING IN THE ABLATION-COOLED REGIME

A THESIS SUBMITTED TO

THE GRADUATE SCHOOL OF ENGINEERING AND SCIENCE

OF BILKENT UNIVERSITY

IN PARTIAL FULFILLMENT OF THE REQUIREMENTS FOR

THE DEGREE OF

MASTER OF SCIENCE

IN

MATERIALS SCIENCE AND NANOTECHNOLOGY

By

Nazifa Tasnim Arony

July 2020

ULTRAFAST LASER-MATERIAL PROCESSING IN THE ABLATION-COOLED REGIME

By Nazifa Tasnim Arony

July 2020

We certify that we have read this thesis and that in our opinion it is fully adequate, in scope and in quality, as a thesis for the degree of Master of Science.

Fatih Ömer İlday(Advisor)

Onur Tokel

Ali Bozbey

Approved for the Graduate School of Engineering and Science:

Ezhan Karaşan
Director of the Graduate School

ABSTRACT

ULTRAFAST LASER-MATERIAL PROCESSING IN THE ABLATION-COOLED REGIME

Nazifa Tasnim Arony
M.S. in Materials Science and Nanotechnology
Advisor: Fatih Ömer İlday
July 2020

Recently, a new regime of material ablation using ultrashort laser pulses has been demonstrated. In this regime, thousands of pulses collectively interact and ablate the material, if the time between subsequent pulses is much less than the time for heat diffusion. Ablation results in the violent ejection from the surface of the material exceeding a critical temperature. As a result, the removal of heat through ablation becomes dominant over thermal diffusion, and this process is called the ablation-cooled laser-material removal. It was shown that ablation efficiency could be significantly increased while simultaneously reducing the pulse energy by several orders of magnitude if the pulses' repetition rate is increased to several GHz. This thesis explores the scaling of the repetition rate up to 100 GHz. Our results indicate that with increasing repetition rate, the efficiency gains of this regime can be maintained along, while further decreasing the pulse energy requirements by 1-2 orders of magnitude. Dramatically, we find that few-nanojoule pulses at 50-100 GHz ablate more efficiently than tens of microjoule pulses at sub-MHz repetition rates. We present systematic results on crystalline silicon and exploratory studies on several technical materials of industrial relevance. The presently reported pulse energies could easily be obtained directly from mode-locked lasers, potentially eliminating the need for costly and complicated laser amplifiers. Therefore, our results are suggestive of a radical transformation of the laser technology required for ultrafast ablation.

Keywords: Laser-material processing, ablation cooling, ultrafast silicon processing.

ÖZET

ABLASYONLA SOĞUTULMUŞ BÖLGEDE ULTRAHIZLI LAZER MALZEMELERİNİN İŞLENMESİ

Nazifa Tasnim Arony
Malzeme Bilimleri ve Nanoteknoloji, Yüksek Lisans
Tez Danışmanı: Fatih Ömer İlday
Temmuz 2020

Son zamanlarda, ultrahızlı lazer darbeleri kullanılarak yeni bir malzeme ablasyon rejimi icat edilmiştir. Bu rejimde, ard arda gelen atimlar arasındaki süre ısı yayılımı süresinden çok daha az ise binlerce atım toplu olarak etkileşime girer ve malzemeyi keser. Ablasyon, malzemenin yüzeyinden kritik bir sıcaklığı aşan şiddetli fırlatma ile sonuçlanır. Sonuç olarak, ablasyon yoluyla malzemeyi hapsolmuş ısının uzaklaştırılması termal difüzyona baskın hale gelir ve bu işleme ablasyon soğutmalı lazer malzemesinin çıkarılması denir. Nabızların tekrarlanma oranı birkaç GHz'e yükseltilirse, gerekli darbe enerjilerinin birkaç büyüklük derecesinde azaltılabilmesine rağmen, ablasyon verimliliğinin büyük ölçüde artırılabileceği gösterilmiştir. Bu tez tekrar oranının 100 GHz'e kadar olan ölçeğini araştırmaktadır. Sonuçlarımız, bu rejimin verimlilik kazanımlarının sürdürülebileceğini, aynı zamanda darbe enerjisi gereksinimlerini 1-2 derece daha da azaltabildiğini göstermektedir. Dramatik olarak, 50-100 GHz'deki birkaç nanojül darbesinin, alt MHz tekrarlama oranlarında onlarca mikrojül darbesinden daha verimli bir şekilde azaldığını görüyoruz. Kristalin silikon üzerinde sistematik sonuçlar ve çeşitli endüstriyel önem taşıyan teknik malzemeler üzerinde keşif çalışmaları sunuyoruz. Şu anda rapor edilen atım enerjileri, doğrudan kip kilitli lazerlerden kolayca elde edilebilir, bu da potansiyel olarak maliyetli ve karmaşık lazer amplifikatörlerine olan ihtiyacı ortadan kaldırır. Bu nedenle, sonuçlarımız ultrahızlı ablasyon için gerekli lazer teknolojisinin radikal bir dönüşümünü düşündürmektedir.

Anahtar sözcükler: Lazer-malzeme işleme, ablasyon soğutma, ultrahızlı silikon işleme.

Acknowledgement

I would first like to thank my respectable thesis supervisor F. Ömer İlday, for his continuous guidance and support during my research. The door to his office was always open (figuratively and literally, there is no lock on his door by design) whenever I had difficulties with my research or had a question about my writing. I feel blessed to have him as my supervisor.

I am especially indebted to my senior colleagues Parviz Elahi, Hamit Kalaycıoğlu, Denizhan Koray Kesim, Özgün Yavuz and Ghaith Makey for their support and helpful feedbacks in various stages during my experiments.

I am also grateful to all members of Ultrafast Optics and Lasers group and all my friends at Bilkent University for their valuable advice, useful comments, remarks and engagement throughout the learning process of this master's thesis.

I would also like to thank the respectable jury members Dr. F. Ömer İlday, Dr. Onur Tokel and Dr. Ali Bozbey, for accepting to be on this committee, and providing their invaluable feedback on this thesis.

I must express my profound gratitude to my parents and my brother for their encouragement during this thesis.

Last but not least, I would like to express my gratitude to my beloved husband, Aqiq Ishraq, who has always been by my side. Without his patience, love, and continuous encouragement, it would be impossible for me to carry on this work and complete my graduate study.

Contents

List of Figures

List of Tables

Chapter 1

Introduction

1.1 Objectives and Review

The foundations of laser technology were established in 1917 when Albert Einstein predicted the mechanism of stimulated emission, which led to the invention of the first fully functional prototype of a ruby laser in the 1960s [1]. This laser was a pulsed laser emitting a deep red-colored beam at a wavelength of 694.3 nm, invented by Theodore Maiman in May 1960. In December of the same year, the first continuous wave (CW) laser was built by a group of scientists at the Bell Communication Laboratories using the He-Ne gas mixture as gain medium for the lasing action that emitted laser light at 1153 nm wavelength [2]. Since the discovery of laser in the 1960s, the physics of laser-material interactions have always been one of the most important fields of scientific research. Shortly after the invention of the first laser, the main application of lasers was in the military rangefinders. Extensive studies have been done since then on laser material processing not only for industrial fields but also for medical applications and scientific research. In this chapter, some notable milestones in the field of laser material processing will be reviewed.

One of the most remarkable inventions in the history of industrial lasers was the first CO_2 CW laser in 1964 [3], which led to the first gas-assisted laser cutting in 1967

using a 300 W pulsed slow flow CO_2 laser [4]. That laser could cut through up to 2.5 mm thick high carbon tool steel and stainless steel at speeds up to 1 m/min. CO_2 lasers became very popular at that time for their lower manufacturing cost than ruby lasers and high-power output. In the next two decades since the 1970s, refinements of CO_2 lasers and invention of Nd:YAG, He-Ne and other types of high-power lasers continued and started gaining recognition for metal cutting, welding, and drilling as scientists in the fields of aeronautics and metal industries realized the importance of laser machining. Upgraded versions of these lasers are still being used commercially for machining. Right after the initial breakthrough of the laser invention, intensive research on the interaction of laser with biological tissue was growing parallelly with other scientific research fields. Zaret et al. [5] reported preliminary studies of retinal and iris lesions in rabbit in 1961 using a pulsed ruby laser. Goldman et al. [6] used a ruby laser to study the interaction of the laser beam with the skin in 1963. They observed that the laser could selectively destroy highly pigmented structures, including hair follicles, leaving little or no evident damage in the underlying white skin layer. Later, this technique became very popular for several skin treatments, including removing birthmarks and tattoos. After the invention of CO_2 and Nd:YAG lasers, series of reports on medical treatments of cancers, bleeding erosions, and recanalization of obstructed bronchi and trachea by tumors were published between the 1970s and 1980s [7–12]. However, the precision, heating effect, and control of energy deposition remained an issue in these types of applications.

In recent years, other than applications in the medical field, the micromachining of different materials using lasers has become a center of attention not only in manufacturing technologies but also in micro and nano-technology. To acquire micrometer-nanometer precision cutting or drilling, better control over the laser parameters is needed. In this field, a widely used term is laser ablation, which refers to the phenomenon of material removal from the bulk using high-intensity laser beams. Research in this area is intense due to its extensive industrial applications, including high-speed micro-drilling, cutting, and micro-structuring. Other than applications in materials science, lasers are successfully used for biomedical applications such as ophthalmology [13–15].

From a broad perspective, lasers used in different fields can be classified into two

main categories- continuous wave (CW) and pulsed lasers. CW lasers operate with continuous output power, whereas pulsed lasers generate laser pulses at a particular pulse repetition rate. Pulsed lasers can be further categorized into long (nanosecond and larger pulse width), short (longer than 10 ps), and ultrashort (typically less than 10 ps and preferably in the femtosecond range) pulses. Early works have been done to explore different regimes of laser ablation, and special attention is given to the ultrashort or ultrafast laser processing due to its short interaction time with the target material which results in controlled and precise micromachining and reduced heat-affected zone in bulk than that produced by the longer pulses [16]. The generation of an ultrashort pulse is not a new concept. Indeed, precursor results were first reported merely six years after the first laser was invented [17]. The first ultrafast laser had picosecond pulses generated from a passively mode-locked Nd:glass laser.

Further advances helped increase the practicality of these early lasers based on solid-state laser technology, including the development of semiconductor saturable absorber mirrors [18, 19]. In recent years, ultrafast lasers have become the most convenient means of laser micromachining. These advantages of the ultrashort pulses over the longer pulses will be reviewed next.

During the material ablation process, the deposited energy is first absorbed, and then part of the bulk material is removed by sublimation. At low powers, the process is dominated by linear absorption. For semiconductors and dielectrics, which have high bandgap energies, low power lasers are not suitable for processing these types of materials. CW lasers or nanosecond lasers cannot compete with the ultrafast lasers in the ablation of a transparent or highly reflective material.

In the past few decades, ultrafast lasers have been widely studied for different applications. These lasers can be used to process a large variety of materials ranging from metals to semiconductors and insulators, from ultra-hard materials to soft living tissue with high precision. Although these lasers have high potential in various fields, they are limited in terms of processing speeds. The pulse repetition rates of high-power ultrafast lasers are in the kHz-MHz range. However, increasing speed is not merely a matter of increasing the repetition rate because there is always plasma formation during the ablation process. The plasma state of the ablated matter, which

contains ionized atoms and electrons, acts as a mirror and reflects the next incoming pulse if the repetition rate is high. This, in turn, reduces ablation efficiency. Ultrafast lasers are energy inefficient. A large portion of the pulse energy is wasted on the ablated material because only a small fraction of the deposited energy contributes to the ablation of the material.

After taking into account all these drawbacks of the ultrafast processing, a novel and efficient solution, namely, the regime of ablation-cooled laser-material processing, has been introduced recently by C. Kerse et al. in 2016 [20]. This regime of laser material processing uses multi-pulses with individual energies far below the threshold energy required to start ablation if only one pulse were used. Nevertheless, they managed to ablate material, in fact, with much higher efficiency because they arrive at the material faster than the diffusion of heat in that material, thus, interacting with the target collectively. To utilize this regime, typically, multi-GHz pulse repetition rates are needed.

1.2 Ablation-Cooled Material Removal

Before starting the discussion on how ablation-cooled regime works, some background information should be provided, which led to the realization of this new regime. Lasers used in the industries for cutting or drilling of metals are high-power CW lasers, and long-pulsed (typically, nanosecond) lasers, mostly due to their low development cost and because relatively low precision is needed in these types of applications [21]. For example, cutting steel or other metals using CW lasers is often done based on melting the metal and blowing the melt away with pressurized gas [22, 23]. Nanosecond pulsed lasers can induce ablation accompanied by the creation of plasma, and allow better control over the processing results [24].

Although the processing quality is better with nanosecond lasers than that with CW lasers, it still creates a large amount of melt and heat-affected zones in the bulk. For more sensitive applications, particularly in scientific research, high precision is often a must for micromachining. In such cases, CW and nanosecond lasers fall

far behind. Ultrafast lasers are the most suitable tools for cutting, drilling, surface-structuring, and even additive manufacturing in the sub-micron scales through a two-photon polymerization technique. However, the trade-off here is that the ultrafast lasers are more expensive and complicated in design. They generally have far slower processing speed than the CW and long-pulse lasers at the same average power. Other than being expensive and slow, there is another issue that makes pulsed ablation energy inefficient, i.e., a large portion of the pulse energy is wasted. This limitation arises from the heat diffusion scheme of a pulse inside the bulk material, which is explained by the Beer-Lambert law [25]. How this law affects laser material processing can be realized more clearly from the following figures.

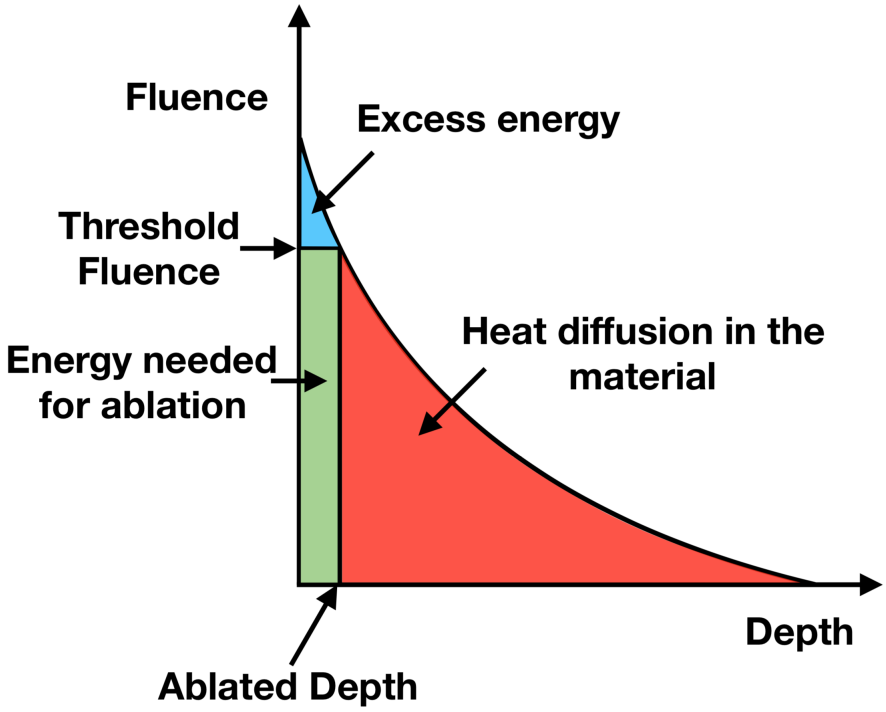

Figure 1.1: Normalized fluence versus depth curve for a single pulse where the fluence exponentially decays inside the bulk, following the Beer-Lambert law. If the pulse fluence is slightly higher than the threshold fluence, ablation occurs but a large portion of the energy is wasted as heat diffusion in the bulk.

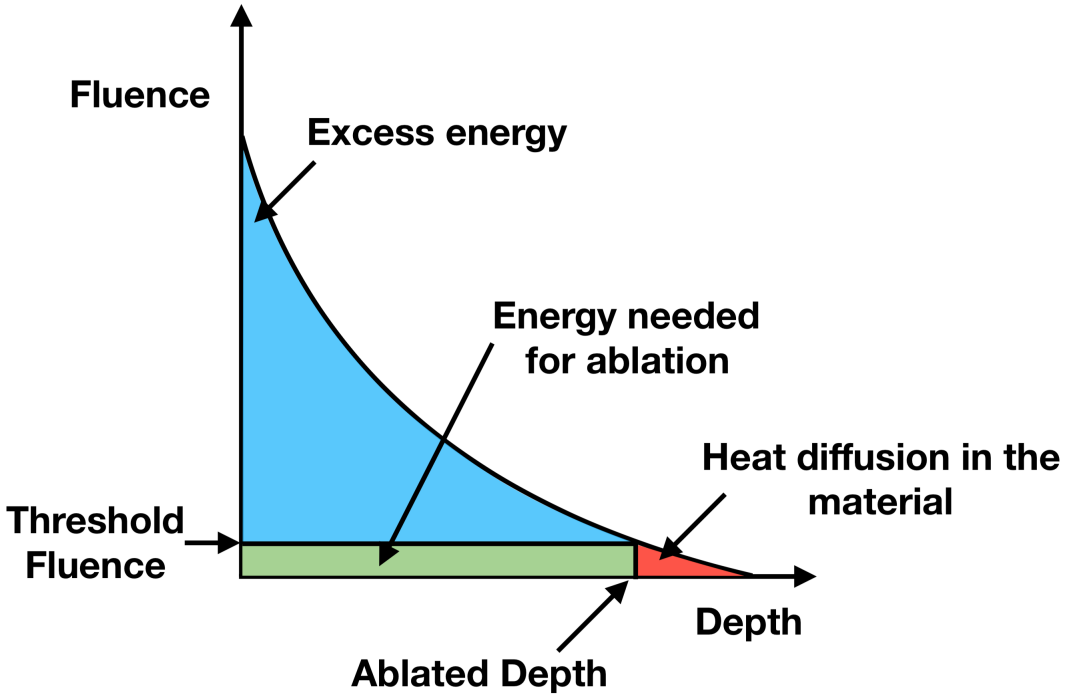

Figure 1.2: Normalized fluence versus depth curve when the pulse fluence is much higher than the threshold fluence in order to get larger ablation depth.

Figure 1.1 depicts one case where the fluence is slightly higher than the threshold fluence (minimum fluence required to start ablation) that results in small ablation depth (green area) but a large amount of heat diffusion (red area), which makes this process energy inefficient. It causes heat-induced damage in the bulk. To increase the ablation depth, pulse fluence much higher than the threshold fluence is needed. In that case (Figure 1.2), the heat diffusion could be reduced (red area), but a large amount of excess energy is wasted (blue area), which does not contribute to ablation. An ideal case can be imagined with a balance between the energy wasted in the ways mentioned earlier (Figure 1.3).

Even though the ultrafast laser processing is energy inefficient, slow, and very expensive relative to CW or nanosecond processing, there is a sizable number of advantages of using it. One notable advantage is that ultrashort pulses can deliver very high peak power localized in an ultrashort time interval. The pulse duration ranges from a few ps to less than a few tens of femtoseconds. This property of ultrashort pulses allows the nonlinear absorption of photons in the material, which makes it

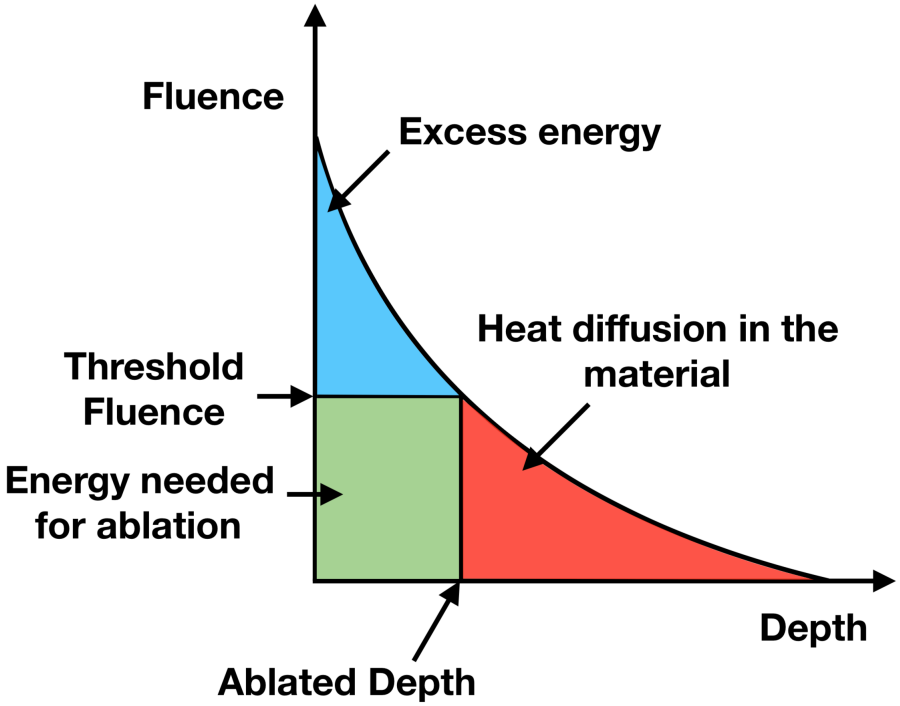

Figure 1.3: Normalized fluence versus depth curve with a balance between the amount of excess energy waste and heat diffusion

possible to ablate materials that have very high bandgap energy and need multiphoton absorption. To employ this process, the use of tightly focusing of the beam and ultrashort pulse durations is necessary to maintain high pulse fluence. The reduction of heat diffusion is thus achieved significantly by the ultrafast processing instead of using the mechanism of heating and melting of the material. So far, we have discussed why the ultrafast regime is preferred for precision micromachining. Next, we will discuss how this processing regime interacts with materials. It is important to get the idea of the physical background of ultrafast processing before moving on to the ablation-cooled regime.

The condition for the high-intensity laser-matter interaction is that the electron oscillation's energy under the laser-generated electric field has to be of the same order of the bandgap energy of the material. It gives a distinct interaction mechanism than that of the low-intensity regime. In the high-intensity regime, plasma evolves when the material is ionized. Increased absorption of the laser light by the generated plasma introduces a high energy density zone at the focal point, responsible for the high

refractive index change. The localization of intense energy in both the spatial and temporal domain assist the progress of controllable precision micromachining.

We already know that, in ultrafast processing, ionization of atoms of the material occurs before the intense plasma formation. Two dominant ionization processes are possible in this case, one is the impact or avalanche ionization, and the other is multiphoton ionization. One of these processes would be dominating, depending on several variables, e.g., pulse duration, wavelength, the intensity of the operating laser, and optical properties of the material at those particular laser parameters. In the avalanche ionization mechanism, the available conduction electrons first gain energy during the oscillations in the laser-generated electric field. These excited electrons can, in turn, excite the valence electrons by collision if they manage to acquire energy higher than the bandgap energy, i.e., when $\varepsilon > \Delta_{\mathrm{gap}}$.

The probability of the occurrence of impact ionization (w_{imp}) is directly proportional to the intensity of the laser and is governed by the following equation.

$$w_{\mathrm{imp}} \approx 2\frac{\varepsilon_{\mathrm{osc}}}{\Delta_{\mathrm{gap}}} \cdot \frac{w^2\, \upsilon_{\mathrm{eff}}}{\upsilon_{\mathrm{eff}}^2 + w^2}, \tag{1.1}$$

where, w, $\varepsilon_{\mathrm{osc}}$ and υ_{eff} are the laser frequency, the electron oscillation energy and the effective collision rate of electrons, respectively. From the equation, it is evident that the probability increases with the square of the laser wavelength. However, after a certain temperature level, the electron-lattice collision rate υ_{eff} saturates at the plasma frequency and frequency dependence of the probability diminishes when $w < \upsilon_{\mathrm{eff}}$ holds. On the other hand, the classical approach must be applicable for both the probability equation and such assumption to be valid. In order to check the conditions, a dimensionless parameter γ can be introduced as

$$\gamma \approx \frac{\Delta\varepsilon}{\hbar w} \cdot \frac{\varepsilon}{\hbar w}. \tag{1.2}$$

From the above equation, we can see that, when $\gamma > 1$, calculation of avalanche ionization can be referred to as a classical phenomenon.

When the excited electron density (n_{e}) reaches to a critical value (n_{c}), optical breakdown takes place. Therefore, at a specific laser frequency, in order to reach the critical electron density for optical breakdown threshold during the interaction of

a material with one pulse, the initial electron density (n_0) must be high enough so that the density of excited electrons can reach the critical density value. The excited electron density and the critical density can be expressed as follows,

$$n_{\mathrm{e}}(t) = n_0 \ 2^{\left(w_{\mathrm{imp}} t\right)} \tag{1.3}$$

$$n_{\mathrm{c}} = \frac{m_{\mathrm{e}}\, w^2}{4\pi e^2} \tag{1.4}$$

Other than the impact ionization, there is another probable phenomenon called the multiphoton ionization, which is a high-intensity regime of ionization. It does not have any certain threshold to reach to start. It depends on the absorption of more than one photon simultaneously. The seed electrons produced by this process can further initiate the impact ionization. The factor that determines which type of ionization will be dominant- tunneling ionization or multi-quantum photo effect, is called the Keldysh parameter. The Keldysh parameter can be defined as the ratio of electron oscillation energy, $\varepsilon_{\mathrm{osc}}$ to bandgap energy, Δ_{gap}. The tunneling ionization dominates when $\varepsilon_{\mathrm{osc}} >> \Delta_{\mathrm{gap}}$. The probability of multiphoton ionization process in both the cases remain unchanged and can be given as

$$w_{\mathrm{imp}} \approx w n_{\mathrm{ph}}^{\frac{3}{2}} \left(\frac{\varepsilon_{\mathrm{osc}}}{2\Delta_{\mathrm{gap}}} \right)^{n_{\mathrm{ph}}}, \tag{1.5}$$

where, $n_{\mathrm{ph}} = \frac{\Delta_{\mathrm{gap}}}{\hbar w}$.

The unique properties of ultrafast laser pulses are that, in this regime, it is possible to separate the time domain for the energy deposition on the material to energize electrons during the pulse and the energy relaxation for the damage. In this case, the energy deposition is a nonlinear process initiated by multiphoton absorption or tunneling absorption that initiates strong impact ionization. The ionization of material creates free-electron plasma that increases the laser absorption until it reaches a critical density [26].

So far, we discussed how ultrafast lasers could reduce heat diffusion into the bulk. Now the question arises on how the high peak power can be achieved in practical applications. Many scientists have addressed this issue, and finally, a well-known solution, called chirped pulse amplification [27], came along in 1985 that was recognized by the 2018 Nobel prize in physics. The main idea of this work was to stretch

the pulses before amplification and compressing them back to much shorter pulses (femtosecond) after the amplification. This invention made high power ultrafast laser processing conceivable, and it opened new possibilities for the thermal damage-free machining of transparent materials and biological samples. However, there remains an issue with the material removal speed of ultrafast lasers. They are not yet optimized for biological applications in the medical fields as the tissue cutting speed is still lower than the operating speed with mechanical surgical tools. As we already know from the literature that in some medical fields, e.g., ophthalmology [28], where the current speed range of processing is acceptable, specialized lasers are being used by the doctors. However, a modification in this process is necessary to implement lasers for high-speed tissue surgery. A way of accelerating the material removal rate, i.e., the amount of material ablated per second, is to increase the pulse repetition rate. High repetition rates can be used until the plasma shielding effect becomes dominant and interrupts the material removal rate.

In the recently demonstrated technique of ablation cooled material processing [19], pulses with a few hundreds of nano joules have been used, and much faster material removal has been obtained by using very high pulse repetition rates, in the order of a few GHz. There have been existing studies on high repetition rate laser material interaction [29, 30], typically in the MHz range, which shows heat-affected zone in the processed area when long bursts of ultrashort pulse trains were used. But the use of a very high repetition rate pulse trains while scaling down the pulse energy makes the ablation cooled regime unique and more efficient than the existing conventional techniques. This regime typically starts from hundreds of MHz pulse repetition rates and continues in the GHz range [19]. The main idea of this method is that, when the time between two pulses is comparable or less than the heat diffusion time in the bulk material, it is possible to remove material without accumulating any heat inside the bulk. With the first few pulses in a large pulse train, the temperature is elevated. As those pulses do not cause any ablation, they can be referred to as sacrificial pulses.

The accumulated heat on the sample surface lowers the ablation threshold of the material. As soon as it reaches the ablation threshold, each next incoming pulse in the train initiates the ablation while removing the excess heat from the material. This

method facilitates the heat left behind from one pulse to reduce the ablation threshold and the excess heat is carried away within the ablated material. This technique eliminates the heating effects while reducing the waste of energy on ablated particles. Due to this dramatic reduction of heat along with the material removal in this process, it is called ablation cooling. The effect of the ablation-cooled regime is shown in figure 1.4. This figure shows how this regime reduces the heat diffusion in the bulk while being very efficient by contributing to very little energy in ablated material. The black line indicates the Beer-Lambert law, and the green area is the maximum ablated depth allowed by this law for a certain pulse fluence. On the other hand, the blue line shows the iteration of a low-energy pulse train that can eventually ablate the same amount of depth as the conventional method. The only difference is that it uses a number of pulses with much lower energy while reducing the energy waste and heat diffusion in the bulk significantly.

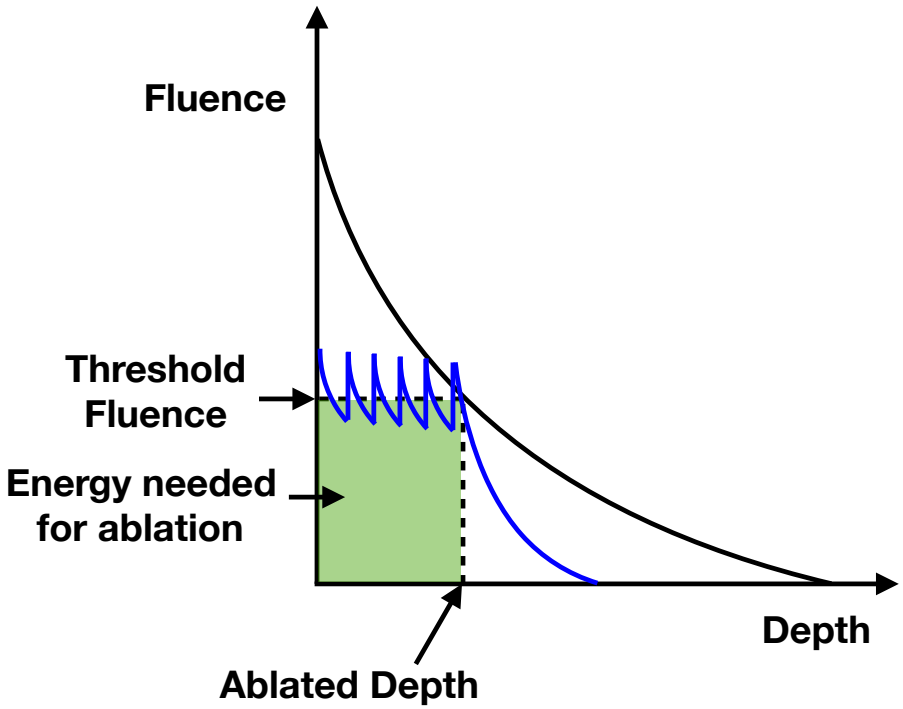

Figure 1.4: Normalized fluence versus depth curve showing the ablated depth achieved by ablation-cooled regime which is similar to that allowed by the Beer-Lambert law for a much higher pulse fluence in the conventional regime.

As the pulse repetition rate increases significantly in the MHz to GHz range, a new challenge arises as maintaining the necessary amount of pulse energy for the train of pulses requires very high average powers, even if the pulse energies are scaled down to μJ-nJ level. To overcome this problem, one solution could be the use of burst mode lasers. These lasers give the facility to achieve pulse energies high enough for ablation with such high repetition rates while reducing the average power. For material processing with burst mode lasers, the burst repetition rates and burst durations are critical parameters for experimental purposes as the variation of these parameters determines the number of pulses used for ablation. The results of material processing with this high repetition rate open new possibilities of high-speed material removal, making it necessary to investigate a deeper region of the ablation cooled regime with a repetition rate as high as 104 GHz.

In this thesis, we follow up on the previously done work and investigate the physics of ablation deeper inside the ablation-cooled regime at 13 GHz, 52 GHz, and 104 GHz

pulse repetition rates. Characterization of monocrystalline silicon at those pulse repetition rates was explored with the ablation depth, ablated volume, and material removal efficiency being the critical parameters for the characterization and optimization of the laser parameters for each repetition rate.

1.3 Properties of Silicon

In this thesis, the material of interest was chosen to be crystalline silicon for various reasons. Most importantly, a sizable amount of work has already been done on silicon, making it convenient to compare the present work with the existing data. It has an abundant supply, and it is an essential material both for industries and for scientific research. As the current study includes the ablation properties of silicon by lasers, it is necessary to know how this material responds to the laser that is being used. The laser used for the experiments has a 1030 nm central wavelength. So, the absorption, transmission, linear and nonlinear parts of the refractive index and other optical properties of silicon at 1030 nm should be studied first. Studies of the interaction of silicon with light show that the absorption coefficient at 1030 nm wavelength is 30.2/cm, and it becomes nearly zero in the spectral range between 1.2 µm to 7 µm. The linear refractive index n_0 is 3.56 at our operational laser wavelength [31].

Chapter 2

Methodology

2.1 Laser Systems

The general structure of the lasers used for the characterization of silicon is shown in figure 2.1. The diagram shows a home-built customized laser system with 13 GHz pulse repetition rate. It is an all fiber-based master-oscillator power-amplifier system. It has Yb-doped fibers emitting laser output with a central wavelength of 1030 nm.

The master oscillator shown in figure 2.1 generates a mode-locked signal at a repetition rate of 100.3 MHz as the seed source. The high GHz repetition rates are achieved using a series of cascaded couplers with a 50% coupling ratio, which is depicted in figure 2.2. It started with the repetition rate of 100 MHz from the oscillator signal and at the end of the series of cascaded couplers, the desired GHz repetition rate was achieved.

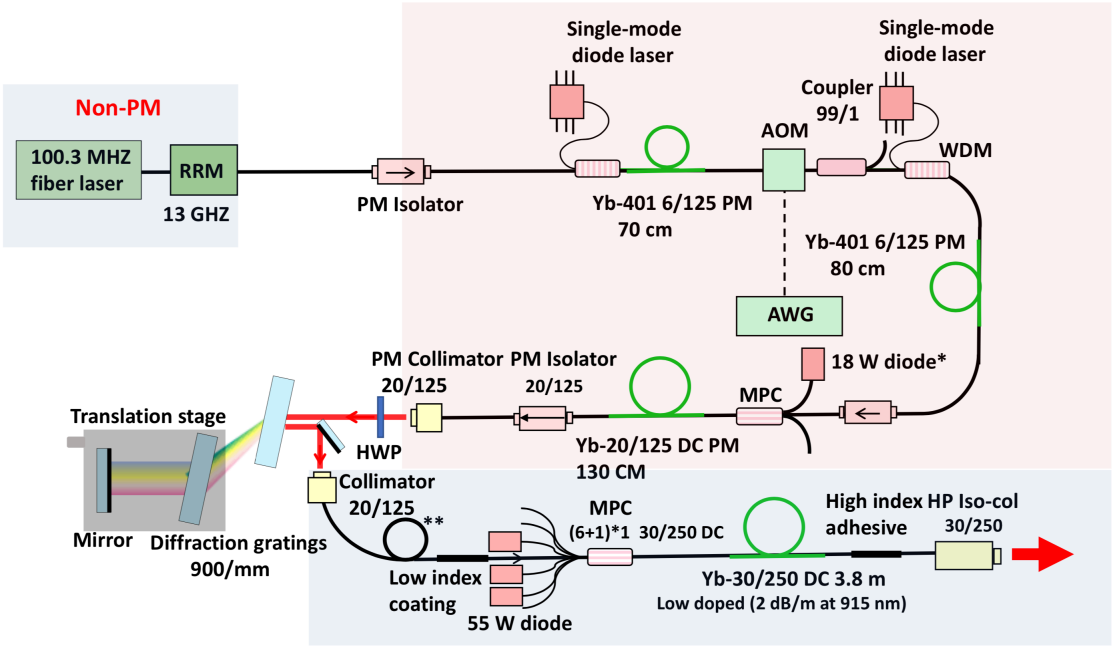

Figure 2.1: Schematic diagram of custom-built 13 GHz laser system.

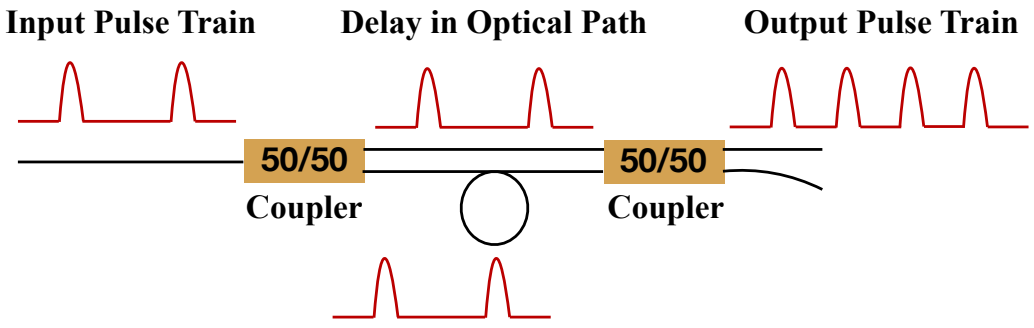

Figure 2.2: Coupling of the repetition rate multipliers for GHz repetition rate output.

At any particular stage, the coupler divides the optical signal into two equal parts. With precise measurements of fiber lengths, the delay between two parts is adjusted so that the output has half the period of the input pulse (Figure 2.2). So, at each stage, this process is repeated to double the pulse repetition rate. This process can be continued until the required fiber length for the adjustment of the delay is long enough to splice with the coupler for the next stage. One of the two output ports from the last stage is connected to the laser system, and the other port is usually used for monitoring.

A cascaded series of eight 50/50 couplers were used to obtain 13 GHz repetition rate. Similarly adding two more couplers, 52 GHz repetition rate was achieved. At 52 GHz repetition rate, the time between two pulses becomes $\sim$19 ps. This means that to increase the repetition rate by a factor of two, i.e., 104 GHz, the optical path delay between the two arms of the repetition rate multiplier should be ~ 3 mm, which is difficult to cut precisely. This is why, 104 GHz repetition rate was achieved using a free-space repetition rate multiplier shown in figure 2.3. A 50/50 free-space beam splitter was used to divide the incoming beam with 52 GHz repetition rate into two parts (blue and orange lines in figure 2.3). The power also became two times less due to the splitting of the beam. Two mirrors were then used at one of the arms (orange line) to adjust the delay between the two parts of the beam. The mirrors were mounted on 2D translational stages with micrometer precision to adjust the path delay. The two beams were then combined using another beam splitter, and the output pulse train was obtained with doubled frequency. As a second 50/50 beam splitter was used to combine the two beams, two ports were obtained with 104 GHz frequency with half the input power. For the experiments, the beam from one of the ports was directed towards the processing station, and the other port was blocked with a beam blocker, or it was used as a monitoring port when needed.

After achieving very high pulse repetition rates, another challenge was faced while maintaining the necessary pulse energy for ablation. The average power required for such repetition rates are extremely high, which is impractical to achieve. The complex laser design and implementation cost would make it undesirable. For example, pulses of only 10 nJ energy repeated at 50 GHz would require the average power of 500 W if a continuous pulse train was used. The burst-mode operation of lasers was adopted

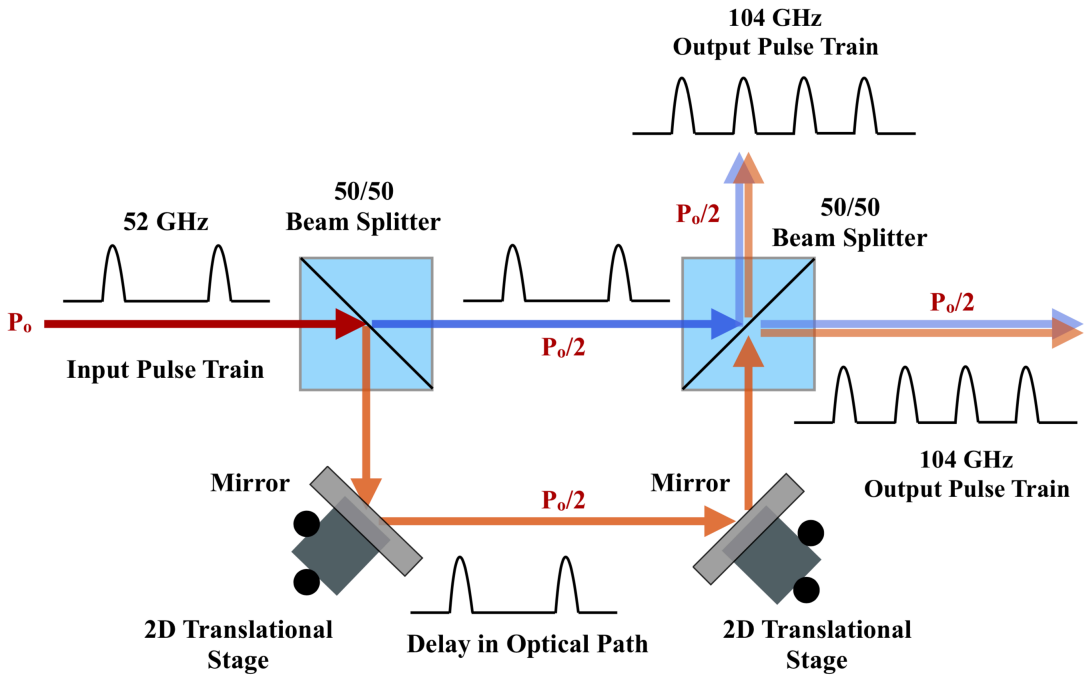

Figure 2.3: Set-up for increasing repetition rates up to 104 GHz from 52 GHz inputs using a free-space repetition rate multiplier.

to overcome this limitation. In this mode of operation, a number of pulses are allowed to pass within a burst envelope, which is again driven at much lower repetition rates [20]. For most of our experiments, we used 100-200 kHz burst repetition rates to reduce the required average power down to a few tens of watts.

Figure 2.4 shows two modes of pulsed lasers- one is burst mode where intra-burst pulses are repeated at much lower burst repetition rates, and in the other mode, the pulses are driven uniformly in a pulse-train. The latter is called the uniform mode of operation.

However, the burst mode lasers require some additional stages in the laser design, e.g., pulsed pumping or pulse pre-shaping. But these additional changes can bypass the need for more complex and costly designs to produce kW level high average power.

As the bursts proceed, the pulses within a burst suffer a decrease in energy due to gain depletion. Due to this gain depletion, the pulses at the end of the burst do not take

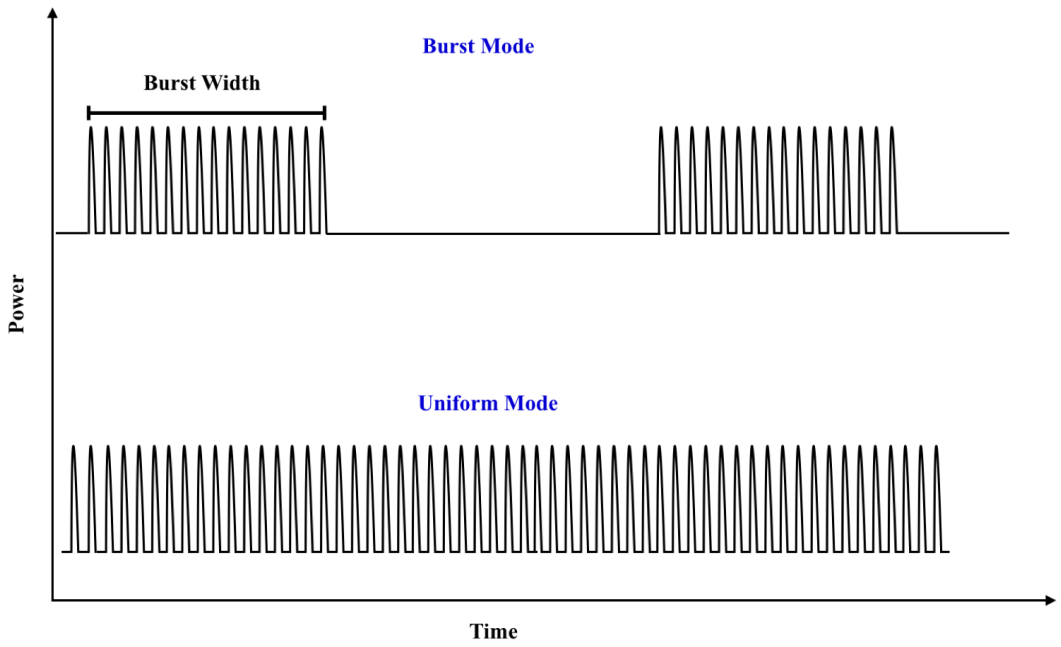

Figure 2.4: Burst mode and uniform mode operation of the pulsed laser.

part in the ablation of material as the energy of the pulse can go below the ablation threshold. In our laser, this problem was solved by following the method described in [32]. Flat burst at the output was thus generated using a calculated envelope of input for the acousto optic modulator (AOM).

As the essential features of the custom-built lasers used in our experiments have been discussed, from here onwards, the laser will be presented simply as a box in simplified diagrams. A simplified experimental setup for the 13 GHz, 52 GHz, and 104 GHz experiments is given in figure 2.5. In this setup, different devices like a power meter, optical spectrum analyzer, oscilloscope, and auto-correlator were used for beam characterization. This characterization setup is necessary to track any change in the beam quality.

All the experiments done at three different pulse repetition rates can be divided into two main groups. One set of experiments was done using a galvanometer scanner, as shown in figure 2.5, and the other group was done with a different high power objective lens. After finishing experiments with the galvanometer scanner, the setup

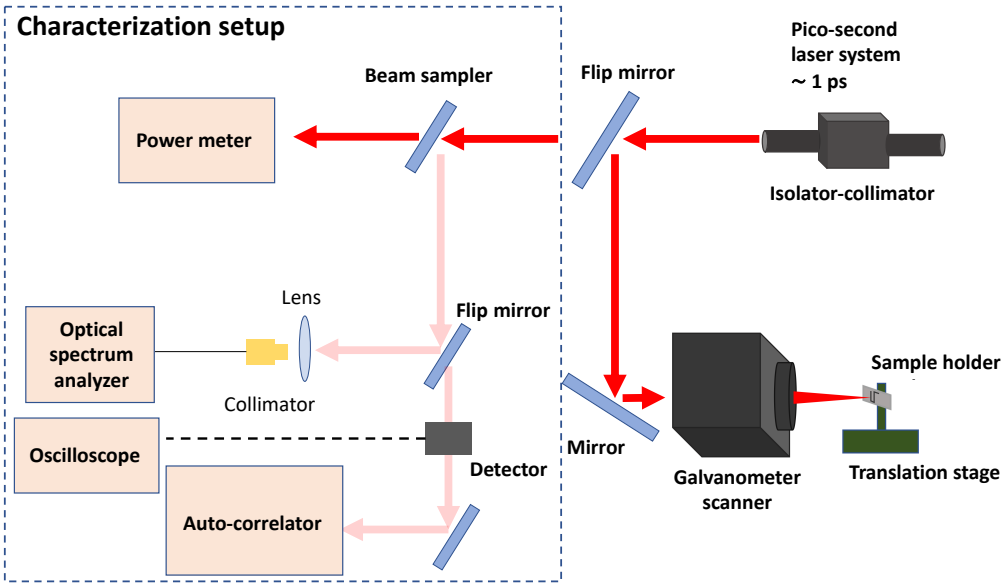

Figure 2.5: Simplified diagram of the experimental set-up for experiments with galvanometer scanner.

shown in figure 2.5 was improved. A Pockels cell (P.C.) was implemented, and the objective lens setup was added along with the galvanometer scanner in the processing station (Figure 2.6).

The older version of the setup shown in figure 2.5 was improved to make use of the laser beam both at high burst repetition rates (by connecting an arbitrary waveform generator with the AOM) and at low repetition rates (by implementing a Pockels cell in the system).

In the improved setup, the output laser is passed through a periscope to decrease the beam's height from the optical table to reduce the effects of small vibrations from the cooling fans or other electronic devices in the surroundings. The laser is then passed through a polarization beam splitter (PBS) to divide it into two parts. One arm can pass through the optical elements and go directly to the galvanometer scanner or the objective lens setup. The other arm goes to the Pockels cell, gets modulated, and then passes through the galvanometer scanner or the objective lens setup, depending on its polarization. The polarization of the beam can be altered using a half waveplate in the path.

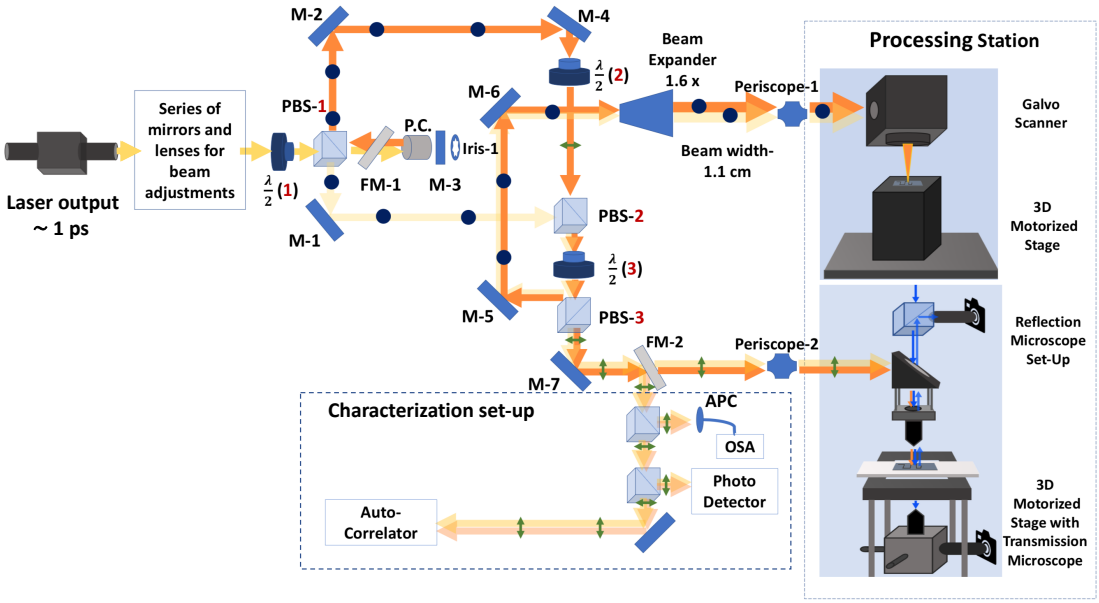

Figure 2.6: Upgraded set-up for the experiments with implementation of Pockels cell and two processing stations.

In figure 2.6, the transparency of the yellow beam is decreased to focus only on the path of one beam as we can send the yellow and orange rays to both the processing stations using two different paths. At first, the input beam enters the first polarization beam splitter (PBS-1). We can see that PBS-1 splits the beam and sends them in two different directions. It lets the laser pass through the Pockels cell (P.C.) if the beam has horizontal polarization. On the other hand, it reflects the beam in 90° if the polarization is vertical (transparent yellow beam with blue dots), and it hits mirror (M-1) and reaches PBS-2. The input beam with horizontal polarization passes through the P.C. after passing through PBS-1, hits a mirror, and comes out of the P.C. with vertical polarization (orange line with blue dots). Then it hits PBS-1. As it now has vertical polarization, it gets reflected from PBS-1 and hits mirror M-2, M-4, and finally passes through PBS-2. These two parts of the beam reach PBS-2 differently, but after that, they both can reach the two processing stations following the same paths.

Pockels cell is an electro-optic device that acts as a voltage controlled waveplate. It consists of an electro-optic crystal which can control the polarization direction of the light passing through the P.C. For our experiments, a constant voltage of 3.2 kV

was applied to the P.C. to use it as a quarter waveplate. It alters the polarization of the incoming beam when it passes through it. In our case, the horizontally polarized incoming beam passes through the P.C. and gets polarized by 45°. At the end of the P.C., there is a mirror (M-3) reflecting the beam again through the P.C. The beam then suffers 45° polarization and finally becomes vertically polarized when it comes out of the P.C. We used the P.C. as a gating device in our setup.

The mirror M-4 deflects the beam towards PBS-3, and from this point by changing the polarization using the half waveplates 2 and 3, the beam either goes to the galvanometer setup or the objective lens setup. As the aperture of the galvanometer scanner used was 14 mm, the beam was expanded to fill the aperture by using a beam expander. Both the processing stations have 3D motorized stages and imaging systems, which are all controlled by a computer.

The methods by which two groups of experiments were done are discussed in sections 2.2 and 2.3. One group was done using a galvanometer scanner and the other group was done using a 3D motorized stage setup and a high power objective lens. For the experiments using galvanometer scanner, the processing patterns were applied on the samples by moving the laser beam using the scanner. The dimensions of the processing area ($< 1\,\mathrm{cm}^2$) was limited by the aperture size of the galvo scanner's lens. For some experiments where a large number of separated ablated spots were needed in a bigger area for measurement purposes, other means of scanning was needed due to the limitations of the size of the scanning area and the scanning speed of the galvo scanner. For those experiments, in order to get more control over the processing scheme, e.g., managing the number of bursts per spot while gating the bursts at frequencies as low as a few hundred hertz, we used the P.C. for the gating of bursts. In this group of experiments, the beam was focused onto the sample using a high power objective lens. We used a programmable 3D motorized stage connected to a computer to move the sample for scanning while the beam remained stationary. Unlike the galvo scanner set-up, here we sent the scanning pattern to the motorized stage using a MATLAB code from the computer. The highest speed of scanning with this motorized stage was 1 cm/s and it was adjusted with the gating frequency of the P.C. in order to achieve desired spacing between the ablated spots. We could scan up to 5 cm in both x and y directions with this stage which allowed bigger processing

areas than the galvo scanner set up. Although this process was slower compared to moving the beam as in the galvo scanner setup, it was a more versatile option. These two methods are described in more detail in the next sections. We also applied nitrogen gas on the sample surface during all the ablation experiments in order to prevent the oxidation of silicon.

2.2 Experiments Using Galvanometer Scanner

The galvanometer scanner used in all these experiments was HurrySCAN II 14 from Scanlab. The experiments were done using an f-θ lens with a 56 mm focal length attached to the galvanometer scanner. The spot size of the lasers at $1/e^2$ for the experiments was measured to be $\sim 23\,\mu m$ with this lens of 56 mm focal length. The Rayleigh length or the confocal parameter was calculated to be $\sim 280\,\mu m$.

$$\frac{\pi \times w_o^2}{\lambda \times M^2} = \frac{3.1416 \times 11.5\,\mu m^2}{1\,\mu m \times 1.5} \approx 280\,\mu m, \tag{2.1}$$

where, M^2 is the beam quality factor for multimode lasers which defines the deformation of the beam from an ideal gaussian beam, w_0 is the radius of the beam at $1/e^2$ and λ is the wavelength of the laser. The spot size and the beam quality factor were measured using a beam profiler.

The single burst experiments using the galvanometer scanner were done with the setup shown in figure 2.5. The sample stage used was a manual 3D stage. The experiments were done on 525 µm ($\pm$ 25 µm) thick monocrystalline silicon wafers. For each experiment, a 1 cm $\times$ 1 cm square pattern was applied to the sample using the galvanometer scanner. This pattern was made to adjust the alignment of the sample and the incoming laser beam. The tilt angle and the height of the sample were adjusted using a manual translational stage. The square also defined the working area. In oreder to fix the focus, first low power was applied, and a low-level of plasma light formation was observed on the square pattern. Then the sample was lifted up and down using the manual stage until a point was reached where the plasma formation was the brightest. That height of the sample was set to be at the focal plane. After

adjusting the focal plane, the processing pattern was applied on the sample using galvanometer scanner. The processing pattern was two parallel lines of 5-8 mm length inside the square.

Due to the galvanometer scanner's processing-speed limitation, the processed craters on the two lines overlap at a 200 kHz burst repetition rate. As the galvanometer scanner's jumping speed was higher than its highest scanning speed for a line, the single-burst craters were formed between the two parallel lines when the scanner jumped from one line to another (Figure 2.7). As seen from this figure, the diagonal line has separated craters ablated with single bursts. The crater profile was viewed, and necessary measurements were taken using a laser scanning microscope (LSM), a highly capable device used to obtain 3D information from the ablated craters. A scanning electron microscope (SEM) was used to assess the surface morphology and the quality of ablation. Also, the LSM measurements were independently verified as follows. Lower burst repetition rates were used to apply a raster pattern, as shown in figure 2.8, and the sample was diced along the processed area and viewed the cross-sections under SEM to take depth measurements. Detailed information regarding imaging and characterization are discussed in section 2.4.

2.2.1 Experiments with 13 GHz Pulse Repetition Rate

For the 13 GHz experiments, the burst repetition rate was 200 kHz. For the single burst experiments, different sets of laser parameters were used to see the effect of burst fluence and pulse energies on ablation characteristics of silicon. 120 nJ, 80 nJ, 50 nJ, 25 nJ, 15 nJ, and 10 nJ pulse energies were used in these experiments. At each pulse energy, six sets of experiments were conducted at six different burst fluences.

The remarkable observation that we made from these experiments was that ablation could be achieved at pulse energy as low as 10 nJ. It shows significant improvement as compared to the typical ablation threshold for silicon, which is around 1 μJ [20] at the same wavelength, pulse duration, and beam size that we used in our experiments. Experiments with the same sets of laser parameters were also conducted at 5 nJ pulse energy, which led to no meaningful ablation other than melting at the

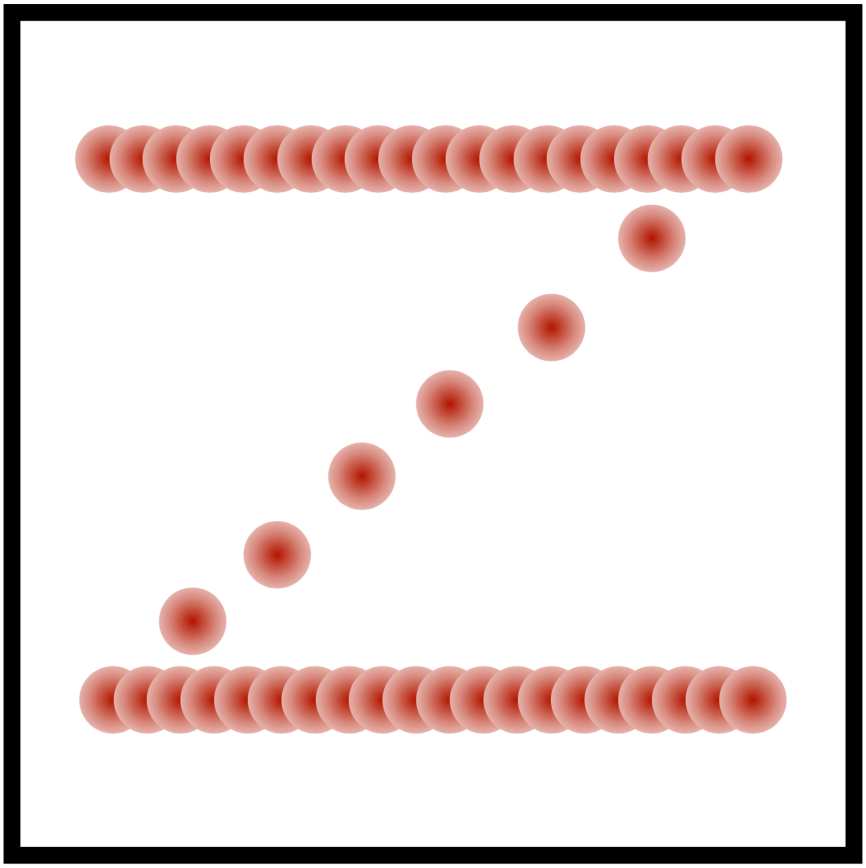

Figure 2.7: Pattern applied for experiments using galvanometer scanner. The black outline is the alignment pattern and each red circle corresponds to incident burst with the illumination spot size of $\sim 23\,\mu m$.

surface, resulting in a dome-shaped structure. We already know that the ablation cooled regime uses the first few pulses to reach the ablation threshold temperature. Thus, at a particular pulse repetition rate, ablation starts at certain pulse energy with a certain number of pulses, which is enough to raise the surface temperature above the threshold and start ablation. As evident from the measurements, there was no ablation for the 5 nJ experiments. The explasnation lies in the discussion above, i.e., 5 nJ energy of the pulses at 13 GHz repetition rate was not high enough to raise the surface temperature above the threshold temperature. Two-temperature model simulations predict that even lower pulse energies would be able to ablate silicon at higher pulse repetition rates [20].

2.2.2 Experiments with 52 GHz Pulse Repetition Rate

As the pulse energy for the ablation threshold could be lowered to 10 nJ for 13 GHz pulse repetition rate, we would expect ablation even at lower pulse energies at higher repetition rates according to [20]. Experiments at 52 GHz pulse repetition rates were thus conducted using the same wavelength and the same pulse duration. The burst repetition rate was 100 kHz. The same galvanometer scanner was used with an f-θ lens of 56 mm focal length with a spot size of $\sim 23\,\mu m$.

For the single burst experiments, different sets of laser parameters were used at 25 nJ, 15 nJ, 10 nJ, 5 nJ, and 3 nJ pulse energies. At each pulse energy, five sets of experiments were conducted at five different burst fluences.

As expected, pulse energy lower than 10 nJ could ablate at 52 GHz repetition rates. Deep ablation was observed at 3 nJ pulse energy from SEM and LSM measurements. Similar experiments were done using 2 nJ pulse energy, but no ablation was observed. We observed a dome-shaped pattern at 2 nJ identical to the one seen on the processed sample at 13 GHz repetition rate with 5 nJ pulse energy.

2.2.3 Experiments with 104 GHz Pulse Repetition Rate

After finishing experiments at 52 GHz repetition rate using the galvanometer scanner, experiments at 104 GHz repetition rate was explored in a similar manner using the same galvanometer scanner and the same processing pattern shown in figure 2.7. Pulse energies used for experiments were 15 nJ, 12 nJ,10 nJ, 5 nJ, and 3 nJ at this repetition rate. At each pulse energies, five sets of experiments were done with different burst fluences. The burst repetition rate was 100 kHz.

The highest ablation depth was observed with processing at 3 nJ pulse energy. Similar experiments were done using 1 nJ pulse energy, but no meaningful ablation was observed at lower burst fluences other than the spike-structures on the surface. We further increased the burst fluence with 1 nJ pulses, and with a fluence of $\sim 40\,\mathrm{J/cm^2}$, we saw irregular spots covered with a large amount of molten material. This implies that this fluence could be very close to the ablation threshold, and with higher fluence, we would expect to observe meaningful ablation with even lower pulse energies. Unfortunately, we could not do experiments with higher fluences due to the technical limitation of our setup.

2.3 Experiments Using 3D Motorized Stage Set-Up

Later on, with the improved setup shown in figure 2.6, another set of experiments was done to explore the ablation threshold fluence at very high repetition rates. Experiments were done with double and multi-bursts using the Pockels cell with a $10\times$ objective lens at 52 GHz repetition rate. Unlike the galvanometer scanner set-up, we used a motorized 3D sample stage to move the sample in a raster pattern. The objective lens used for these experiments had a 20 mm effective focal length, and the spot size was $\sim 10\,\mu\mathrm{m}$. These experiments were done by keeping the pulse energy constant at 3 nJ while changing the burst fluence by changing the number of pulses in a burst. For longer bursts with a large number of pulses, double burst experiments were conducted, and for shorter bursts, i.e., a smaller number of pulses, 10-50 bursts per spot were used. The measured depth was divided by the number of bursts used

to ablate one crater in order to calculate ablated depth per burst. As the best efficiency at 52 GHz experiments with the galvanometer scanner was found to be at 3 nJ pulse energy, the pulse energy for $10\times$ objective experiments was chosen to be 3 nJ. As the spot size was around two times less with the $10\times$ objective than that of the galvanometer scanner, the fluence increased by a factor of 4. In these experiments, ablation was observed with the number of pulses as low as 300 at 3 nJ pulse energy. We achieved extremely deep ablation using bursts of 25,000 pulses. The ablation depth was around ~ 25 µm, and we did not observe a significant increase in ablation depth with a further increase in pulse number. The reason behind this saturation in ablation depth could be that the ablated particles were unable to get out of the crater when the ablated depth was ~ 25 µm, given the crater diameter was around 12-13 µm. For the $10\times$ objective experiments, a computer-controlled 3D stage was used. As the crater diameter was smaller than the ablation depth of the craters processed with longer bursts, the LSM measurements gave noisy signal-like structures in the ablation depth profile. The reason behind this unreliable depth information from LSM data could be that the small diameter of the crater scattered light, which prevented proper imaging inside the crater. Thus, we used SEM to obtain reliable depth information.

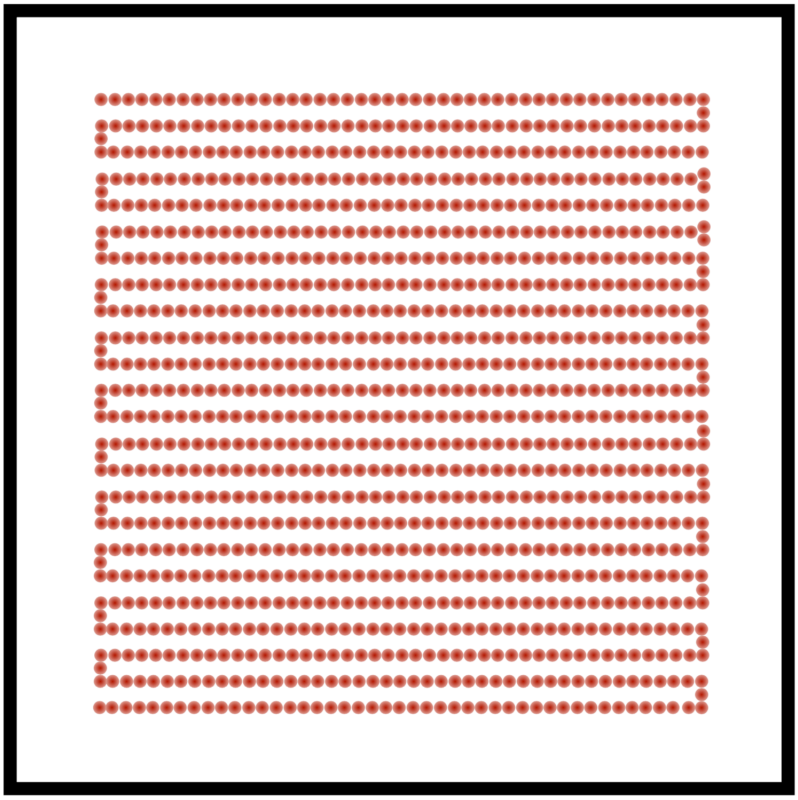

Figure 2.8: Raster pattern applied for experiments using the 10× objective and the motorized stage.

For this purpose, thousands of craters were formed in a raster pattern on a 1 cm × 1 cm square area, as shown in figure 2.8. The sample was then broken in segments using the diamond-tip cutter manually. The reason for using a larger processing area with thousands of processed holes was to increase the probability of finding the craters on one broken segment. The cross-section of the sample segments was then viewed using SEM, and the crater-depth was measured from the SEM images. The consistency in the SEM and LSM measurements was confirmed by measuring samples with relatively lower depth using both these methods.

2.4 Imaging and Data Collection

Two main imaging techniques were extensively used for surface quality assessments, data collection, and measurements for the processed samples. These techniques are confocal laser scanning microscopy (LSM) and scanning electron microscopy (SEM).

2.4.1 Scanning Electron Microscopy (SEM)

After processing, the samples were first rubbed with ethanol using a lens cleaning tissue. Then, each sample was cleaned using an ultrasonic cleaner for 10-15 minutes. Cleaning the samples carefully plays an important role in the imaging and data collection from the processed samples. Otherwise, some ablated material might cover important features of the processed area. Figure 2.9 shows the comparison of the SEM image of samples before and after cleaning with the ultrasonic cleaner.

SEM is one of the best imaging devices to assess the surface morphology of the sample, and we analyzed the surface quality of the ablated samples primarily from SEM images. The SEM device we used was FEI Quanta 200 FEG. In order to take SEM images, the sample must be small enough for the sample holder and must be electrically conductive. Usually, there are different ways of making the sample surface conductive if the sample is a semiconductor or insulator. Sputter coating with gold or gold-palladium alloy can be used to make the surface conductive. This is necessary for insulators. For semiconductors, conductive carbon tapes can also be used other than sputter coating. The second method was used for our silicon samples.

From figure 2.10, we can even analyze the surface inside the ablated crater from the magnified image. The outer ring structure around the ablated crater was formed due to our laser's gaussian beam shape. The tails of the gaussian beam melts part of the surface. This problem could be solved by implementing a top-hat beam shape.

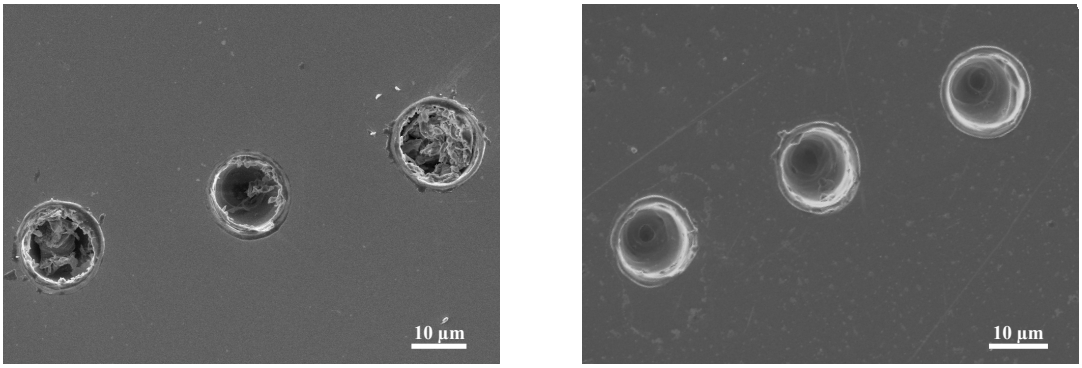

Figure 2.9: SEM image of a processed sample before (Left) and after (Right) cleaning the sample using an ultrasonic cleaner for 15 minutes.

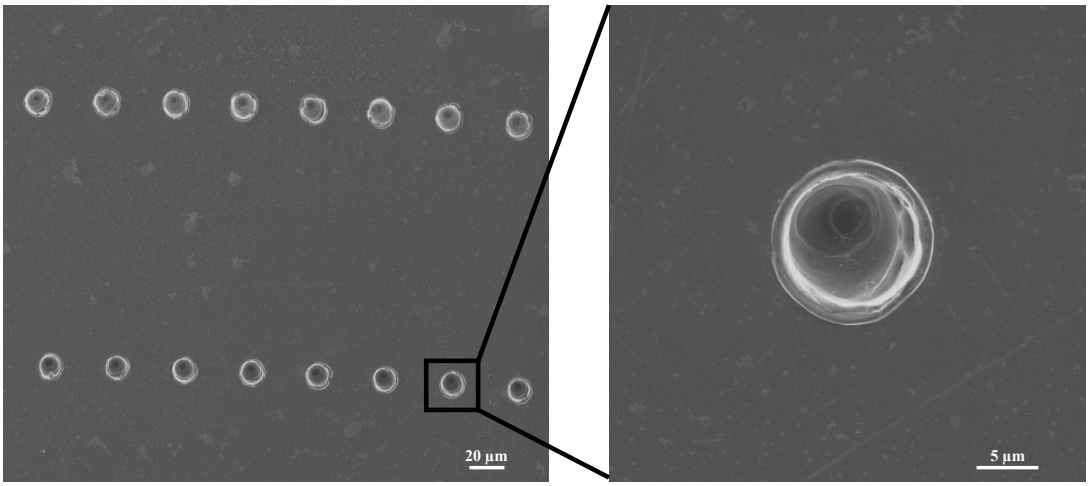

Figure 2.10: SEM image of a processed sample with 3 nJ pulse energy at 52 GHz repetition rate.

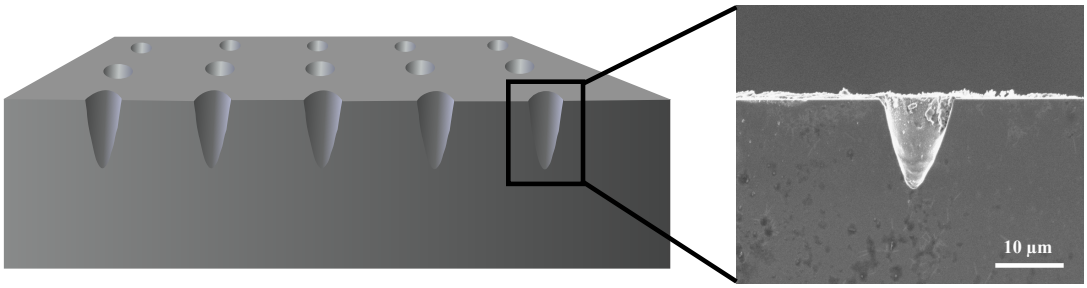

Figure 2.11: Schematic of a diced silicon sample and an SEM image of a diced sample viewed from the cross-section.

We diced some of the processed samples to measure the ablation depth from the craters' crosssections, as shown in figure 2.11. These cross-sectional measurements were also used to verify the measurements taken from laser scanning microscopy, which will be discussed in the next section.

2.4.2 Confocal Laser Scanning Microscopy (LSM)

We utilized laser scanning confocal microscopy as it is one of the most useful techniques to characterize and collect the 3D profile information of the processed samples. The confocal LSM used in our measurements was VK-X 100 from Keyence. The 3D profile of an ablated crater viewed in LSM is shown in figure 2.12. We can also obtain depth and volume data from LSM images by using suitable measurement softwares.

We verified the reliability of the LSM measurements by using SEM, which was discussed in the previous section. The method of ascertaining depth information using SEM is shown in figure 2.11. We found that the variation in measurements in these two methods is less than 1 percent.

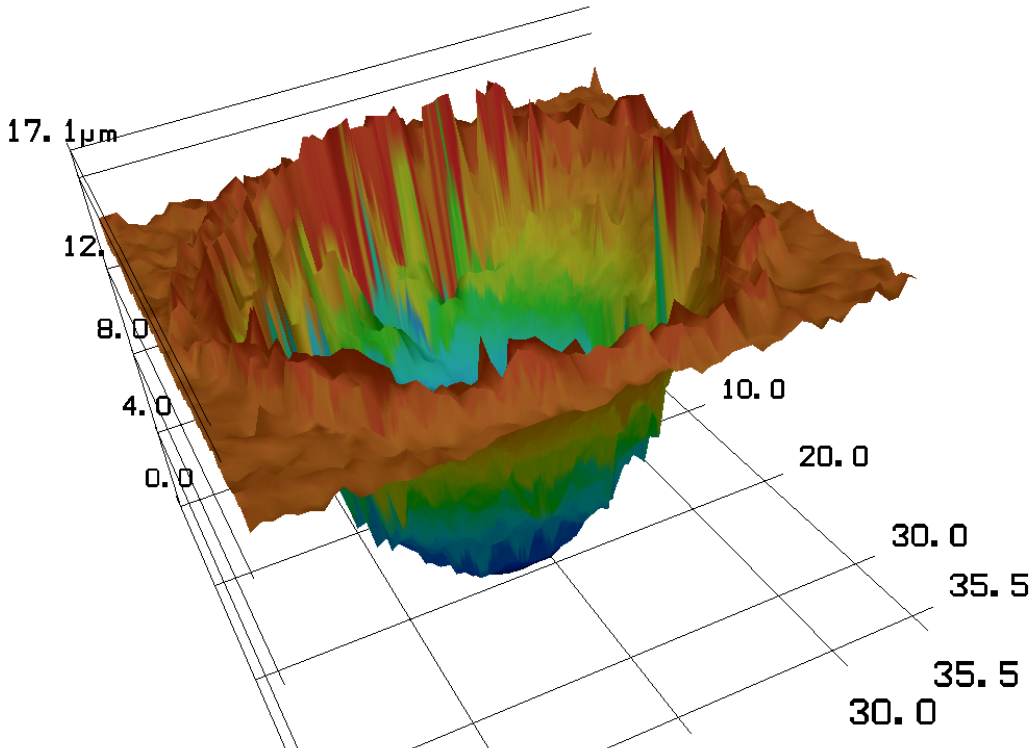

Figure 2.12: 3D profile of an ablated crater viewed in LSM.

Chapter 3

Results and Discussion

In this chapter, the results of the experiments done on silicon using all three laser systems are presented and the implications of the gathered results are discussed in detail.

3.1 Results of the Experiments with 13 GHz Repetition Rate

At 13 GHz pulse repetition rate, 10 nJ to 120 nJ pulse energies have been used for six different sets of burst energies starting from 32 µJ to 240 µJ. All the experiments were done using a single burst per spot. The number of pulses was varied by changing the burst duration by sending the gating signal to the AOM using an arbitrary waveform generator. The highest number of pulses used in 13 GHz experiments was 24,000 pulses per burst for 10 nJ pulses. The burst fluence was varied by changing the number of pulses in a burst, for each pulse energy setting.

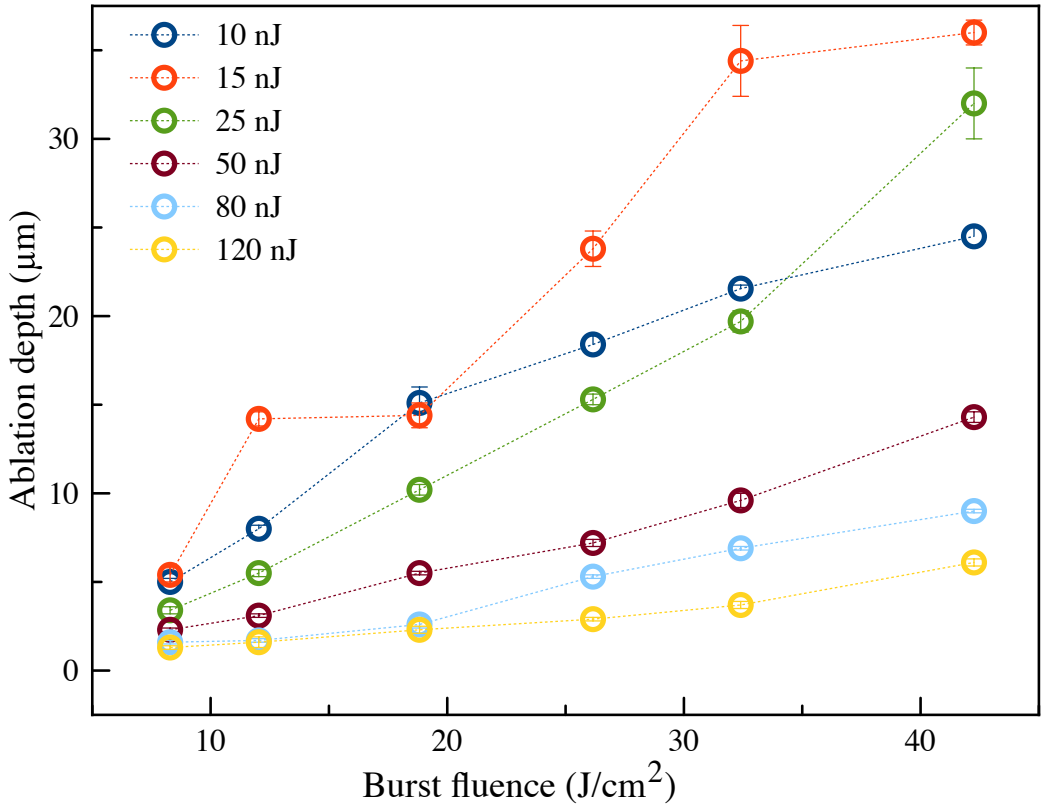

Figure 3.1: Ablation depth versus burst fluence curves at six different pulse energies at 13 GHz pulse repetition rate.

For each pulse repetition rate, there is a pulse energy which yields the best ablation efficiency. In the case of 13 GHz, two pulse energies gave similar results: 15 nJ and 25 nJ. For 15 nJ pulse with 19 J/cm^2 burst fluence, the efficiency of ablation was 2.4 mm^3/Wmin and it remained the same even when the burst fluence was increased to 26 J/cm^2 and 32 J/cm^2. When fluence was further increased, the efficiency dropped to 2.2 mm^3/Wmin at 42 J/cm^2. For 25 nJ pulse energy, the highest efficiency of 2.5 mm^3/Wmin was achieved with 26 J/cm^2 burst fluence. The results of all the sets of experiments at 13 GHz repetition rate using a galvanometer scanner with 23 µm spot size can be seen in figure 3.1 and figure 3.2. Figure 3.1 shows the ablated depth versus fluence curves at six different pulse energies. From this graph, we can see that although we could achieve ablation at 10 nJ pulse energy, the highest crater depth of 36 µm was achieved with 15 nJ pulse energy at 42 J/cm^2 burst fluence. As we increased pulse energy, ablation depth dropped, which could be due to the plasma shielding effect.

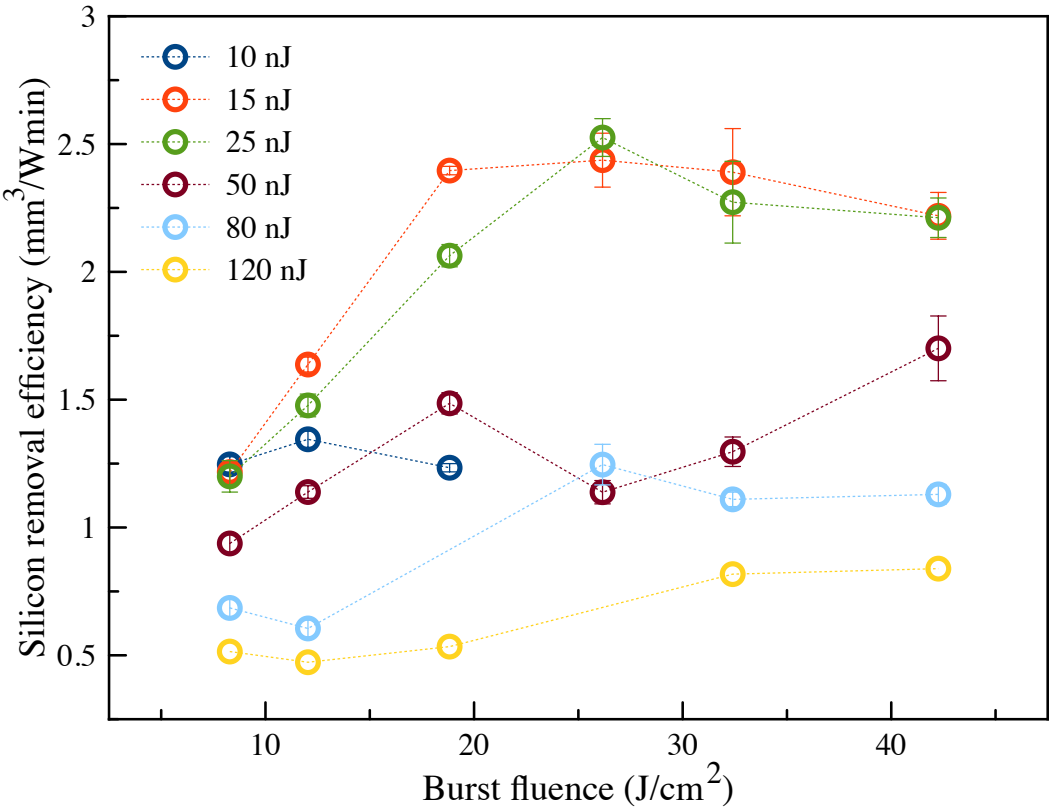

Figure 3.2: Silicon removal efficiency versus burst fluence curves at six different pulse energies at 13 GHz pulse repetition rate.

3.2 Results of the Experiments with 52 GHz Repetition Rate

At the 52 GHz pulse repetition rate, 3 nJ to 25 nJ pulse energies have been used for five different sets of burst fluences starting from 8 J/cm^2 to 32 J/cm^2. We also did experiments with 2 nJ pulses, but no ablation was observed. In the case of 52 GHz, the most efficient pulse energy was found to be 3 nJ. One notable point is that no ablation was observed with 3 nJ pulse energy at 8 J/cm^2 fluence. For this parameter, spikes were observed at the irradiated points on the silicon sample. The results of all the sets of experiments at 52 GHz repetition rate using a galvanometer scanner with 23 µm spot size can be seen in figures 3.3 and 3.4. Figure 3.3 shows ablated depth versus fluence curves for different pulse energies. The highest ablated depth obtained at this repetition rate was 32 µm with 3 nJ pulses at a fluence of 32 J/cm^2. Figure 3.4 shows silicon removal efficiency versus fluence curves for five different pulse energies. The highest efficiency of 1.9 mm^3/Wmin was obtained with 3 nJ pulse energy at 26 J/cm^2 fluence. As we increased the fluence, the efficiency dropped at 3 nJ pulses. This could be due to the fact that, although at higher fluences we increased burst energy, the ablated volume did not increase in the same proportion, which means that after a certain depth, the ablated material could not come out of the crater and resulted in saturation in volume and thus in silicon removal efficiency.

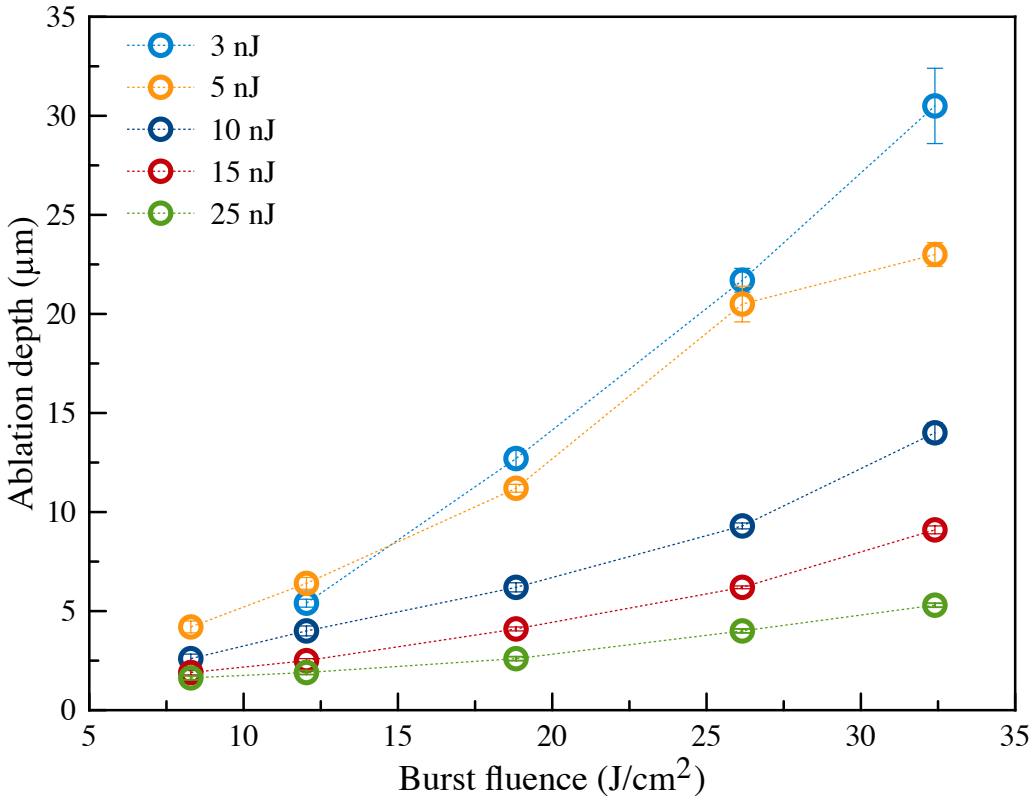

Figure 3.3: Ablation depth versus burst fluence curves at five different pulse energies at 52 GHz pulse repetition rate.

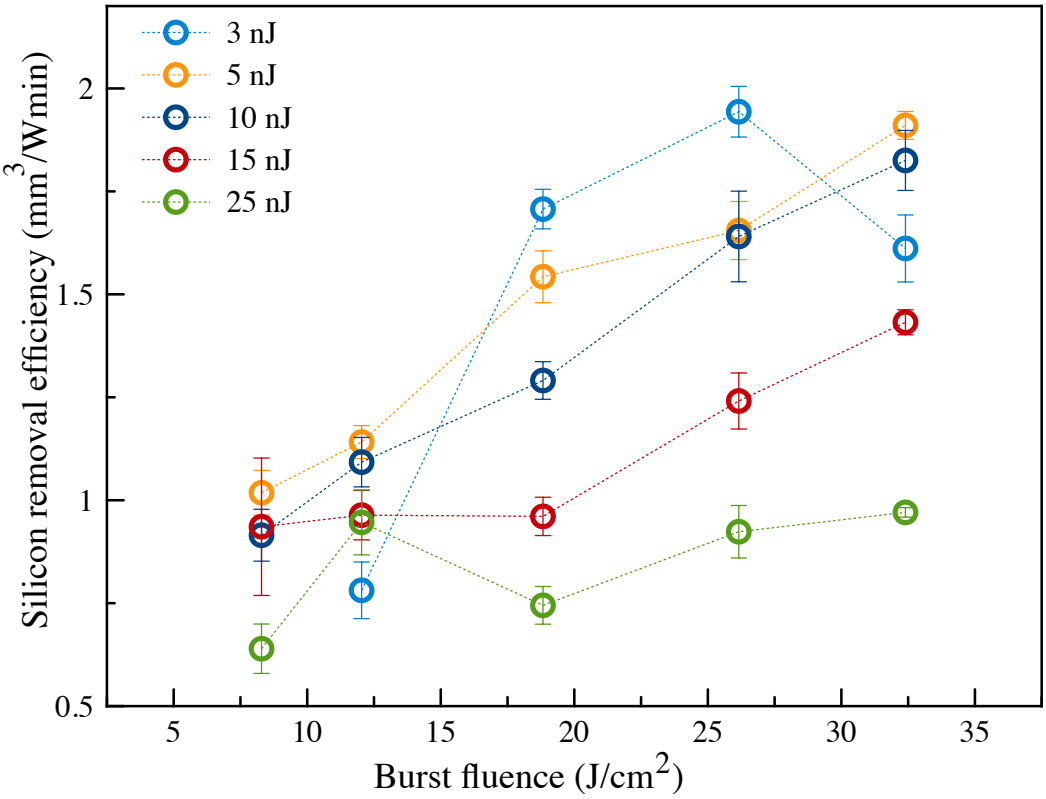

Figure 3.4: Silicon removal efficiency versus burst fluence curves at five different pulse energies at 52 GHz pulse repetition rate.

Now, one of our goals was to analyze the ablation threshold at very high repetition rates. In order to do so, we did a set of experiments at the 52 GHz repetition rate using a 10× objective lens. The spot size of the beam was ∼10 µm, which made it possible for us to use four times higher fluence than what we could use with the galvanometer scanner as the spot size was two times larger. In these experiments, the Pockels cell was used as a gating device to use multi-burst experiments with lower frequencies with the objective lens setup. A much lower frequency as 200 Hz was used, which was necessary to use with this setup as the highest scanning speed of the motorized stage was around 7 mm/s. The highest number of pulses used in these experiments was 30,000 pulses starting from the lowest number of 300 pulses in one burst. The arbitrary waveform generator limited the lowest number of pulses. A burst of 30,000 pulses corresponds to a fluence of 115 J/cm^2, and with 300 pulses, the fluence is 1.2 J/cm^2 with 3 nJ pulses. We could obtain a depth of 35 nm/burst at the lowest fluence of 1.2 J/cm^2 with 300 pulses/burst. As we can see in figure 3.5, the depth kept

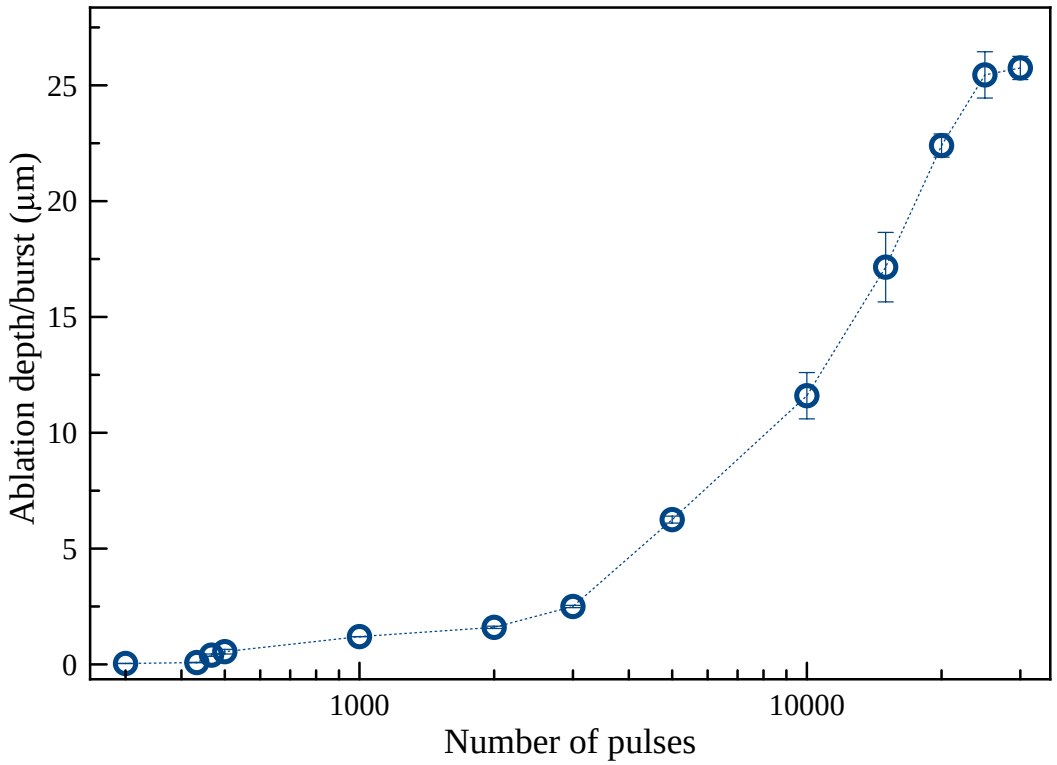

Figure 3.5: Ablation depth per burst with different number of pulses in a burst keeping the pulse energy constant at 3 nJ. These experiments were done at 52 GHz repetition rate using a 10× objective lens. The spot size of the beam was ∼ 10 µm.

increasing very slowly as the pulse number was increased up to 2000 pulses/burst at a fluence of 7.6 J/cm^2. After this point, the depth increased sharply, and at around 25,000 pulses, the depth started to saturate with 25 µm crater depth. Even after we increased the number of pulses to 30000, the depth did not increase further.

3.3 Results of the Experiments with 104 GHz Repetition Rate

At 104 GHz pulse repetition rate, 3 nJ to 15 nJ pulse energies were used for five different sets of burst fluences starting from 8 J/cm^2 to 32 J/cm^2. The results of all the sets of

experiments at 104 GHz repetition rate with $\sim 23\,\mu m$ spot size can be seen in figures 3.6 and 3.7. Figure 3.6 shows the ablation depth versus fluence curves at different pulse energies. We can see that the highest depth of 21 µm was obtained with 3 nJ pulse energy at 32 J/cm^2 burst fluence. At higher pulse energies, the ablation depth was lower, which is also a similar trend we observed at the two other repetition rates.

Figure 3.7 shows the silicon removal efficiency at different pulse energies with increasing burst fluence. From the curves, we can see that the highest efficiency was 1.7 mm^3/Wmin, which was achieved both at 3 nJ pulses with 120 µJ burst energy and 5 nJ pulses with 160 µJ burst energy. Higher pulse energies give lower values of efficiency and ablation depth than the lower pulse energies. This result confirms that at higher repetition rates, lower pulse energies provide the best results, and with higher pulse energies, the shielding effect increases. However, at 104 GHz repetition rate, some experiments were also done at 1 nJ pulse energy with 160,000 pulses in a burst, which resulted in spikes on the sample surface, leading to no meaningful ablation. This implies that 1 nJ pulse energy with 1 ps pulse duration was not high enough to reach to the threshold temperature even though very large number of pulses were used in a burst.

The highest efficiency was 1.7 mm^3/Wmin, which was achieved both at 3 nJ pulses with 26 J/cm^2 burst fluence and at 5 nJ pulses with a fluence of 32 J/cm^2. One notable point is that at this repetition rate, ablation was observed at 3 nJ with 10667 pulses, which was the smallest number of pulses used in all 3 nJ experiments at both 52 GHz and 104 GHz. For this parameter, spikes were observed at 52 GHz, but ablation was achieved at 104 GHz.

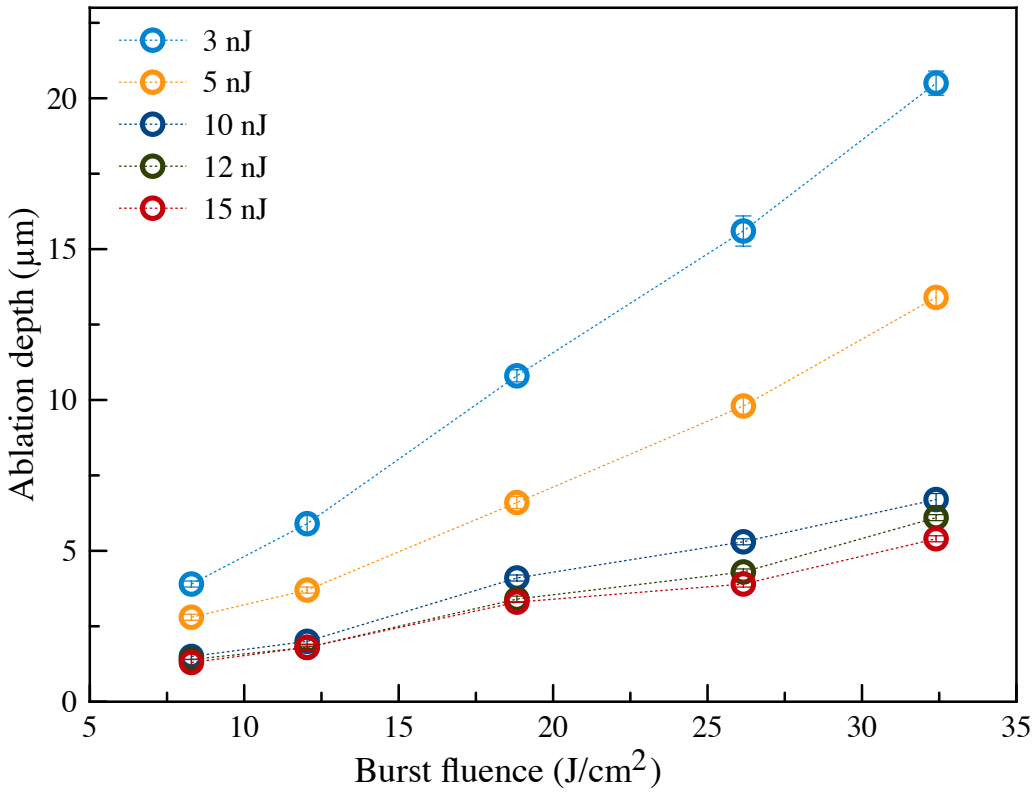

Figure 3.6: Ablation depth versus burst fluence curves at five different pulse energies at 104 GHz pulse repetition rate.

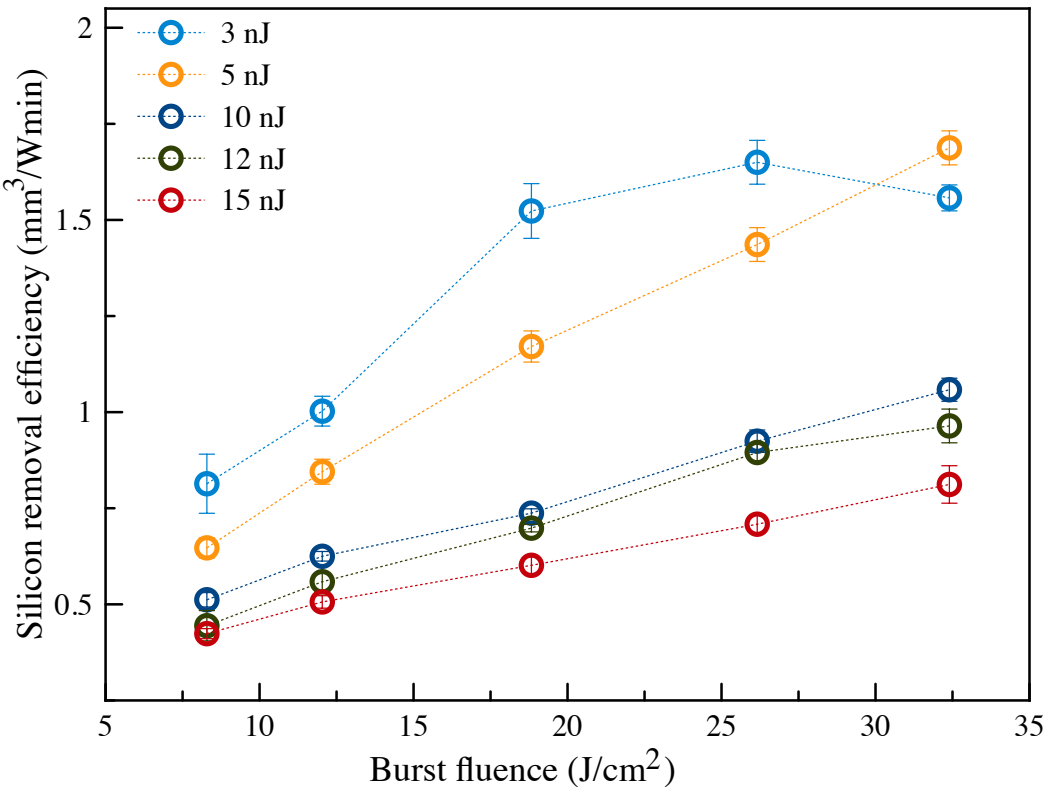

Figure 3.7: Silicon removal efficiency versus burst fluence curves at five different pulse energies at 104 GHz pulse repetition rate.

3.4 Efficiency Comparison

Ablation efficiency is a measure of the ablation capability of a laser. Consequently, we explored the ablation of silicon deep inside the ablation cooled regime with 13, 52, and 104 GHz pulsed lasers. To have an idea about the improvements in ablation efficiency in this regime with our results, we can now look at the bigger picture and compare the present work with the state of the art of ablation cooled regime [19]. We have also made a direct comparison of our work with the traditional ablation regime using a femtosecond pulse laser. The comparison in the ablation efficiency of the present work with the previous work [19] and the traditional regime is shown in figure 3.8.

From [19], we find that the highest ablation efficiency on silicon at 3.5 GHz pulse repetition was 0.6 mm^3/Wmin. We obtained the highest silicon removal efficiency of 2.5 mm^3/Wmin at 13 GHz pulse repetition rate, which is ~ 4 times higher than the state of the art. A notable observation here is that with increasing repetition rate, we could achieve very high ablation efficiency while decreasing the pulse energy by a factor of ~ 50 than what was used in [19].

In order to show the magnitude of our improvement in ablation efficiency, we also performed experiments in the traditional ultrafast regime. We used a pulse laser with 300 fs pulse duration and 50 kHz repetition rate on a silicon sample. We obtained the highest silicon removal efficiency of 0.2 mm^3/Wmin using 40 µJ pulse energy. In contrast, we used pulse energies in the nanojoules range to obtain very high efficiencies at repetition rates as high as 100 GHz. Our results show that we could increase efficiency by a factor of 12 while decreasing the pulse energy more than ten thousand times lower than the traditional regime. This effectively demonstrates that as we go deep inside the ablation cooled regime, we can achieve ablation at a few nano joules of pulse energies, which could be achieved directly from mode-locked lasers, potentially eliminating the need for costly and complex power amplifiers.

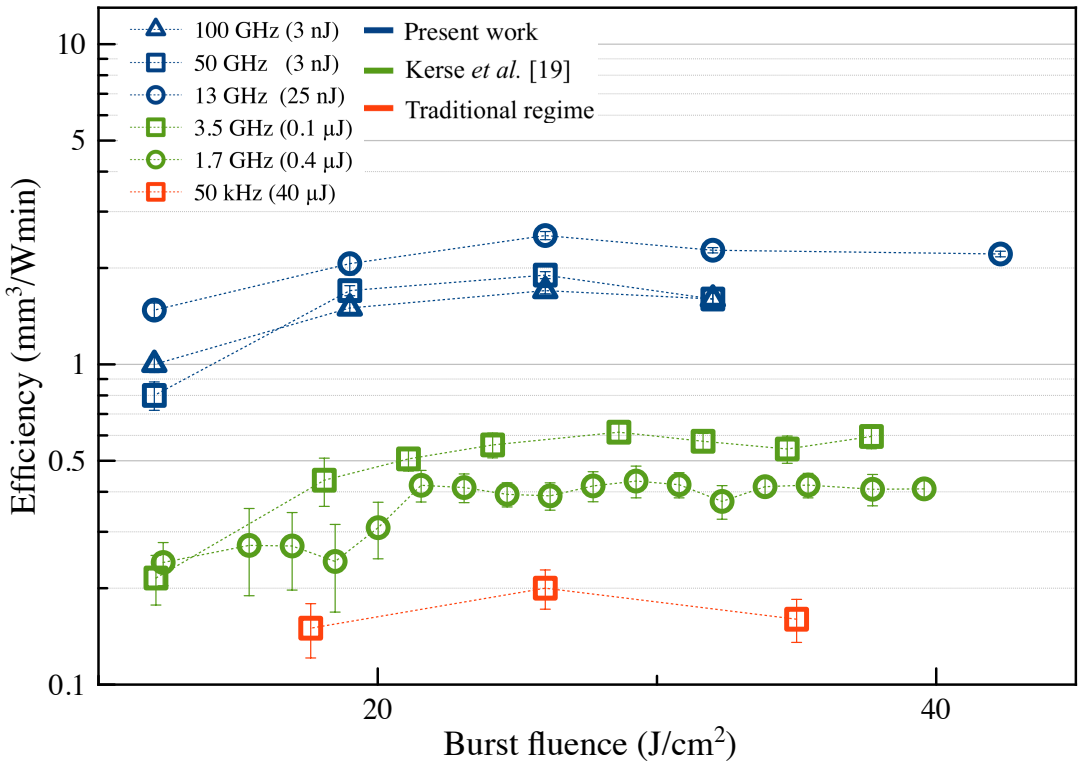

Figure 3.8: Ablation efficiency versus burst fluence comparison between present work with the state of the art [19] and traditional ultrafast regime.

Aside from obtaining very high ablation efficiency at 13 GHz repetition rate, we made an interesting observation as we further increased the repetition rates. We saw that at much higher repetition rates, the efficiency slightly decreases. Ablation efficiency is directly affected by the number of sacrificial pulses that are used to raise the temperature of the target material. As we increase the pulse repetition rate, we also scale down the pulse energy to avoid the plasma shielding effect. We can hypothesize that this decrease in efficiency could be due to the fact that, as the repetition rate is increased, the number of sacrificial pulses also increases for the sake of raising the temperature of the material to the ablation threshold temperature. With an increasing number of non-ablating pulses with lower energies, we would expect a drop in the ablation efficiency as the pulses' peak power would also drop. In order to preserve high efficiency with high pulse repetition rates, one possible solution could be preserving the necessary peak power by reducing the pulse duration at least by the same factor as the increasing repetition rates. In all our experiments, we used ~ 1 ps pulse

duration with different repetition rates, and we observed a slight drop in efficiency. To experimentally back up this hypothesis, a more detailed study on this matter is necessary.

3.5 Speed of Ablation

As we continued to increase the repetition rate, we made a curious observation, where we saw a significant increase in the ablation speed at much lower fluences. The linear speed of ablation or the ablation speed can be defined as the ratio of the ablation depth, d_{ablation} per burst to the burst duration, τ_{burst},

$$v_{\text{ablation}} = \frac{d_{\text{ablation}}}{\tau_{\text{burst}}}. \tag{3.1}$$

The ablation speed refers to how fast a crater of a certain depth is ablated by a certain number of pulses. We care about the ablation speed because it is also a direct measure of how fast the material is being drilled. In this thesis, the limit of the speed that could be achieved by the currently available lasers in our lab was investigated. For this purpose, we calculated the speed of ablation at 13, 52, and 104 GHz repetition rates at different pulse energies.

Figures 3.9-3.11 show the ablation speeds calculated from the experiments at 13, 52, and 104 GHz repetition rates. At 13 GHz repetition rate, the highest speed of 60 m/s was obtained with 120 nJ pulse energy at 42 J/cm^2 burst fluence. A similar ablation speed was obtained using 25 nJ pulse energy at 52 GHz repetition rate at 32 J/cm^2 fluence. The highest speed of 67 m/s was achieved at a 104 GHz repetition rate with a much lower pulse energy of 15 nJ and a much lower fluence of 19 J/cm^2.

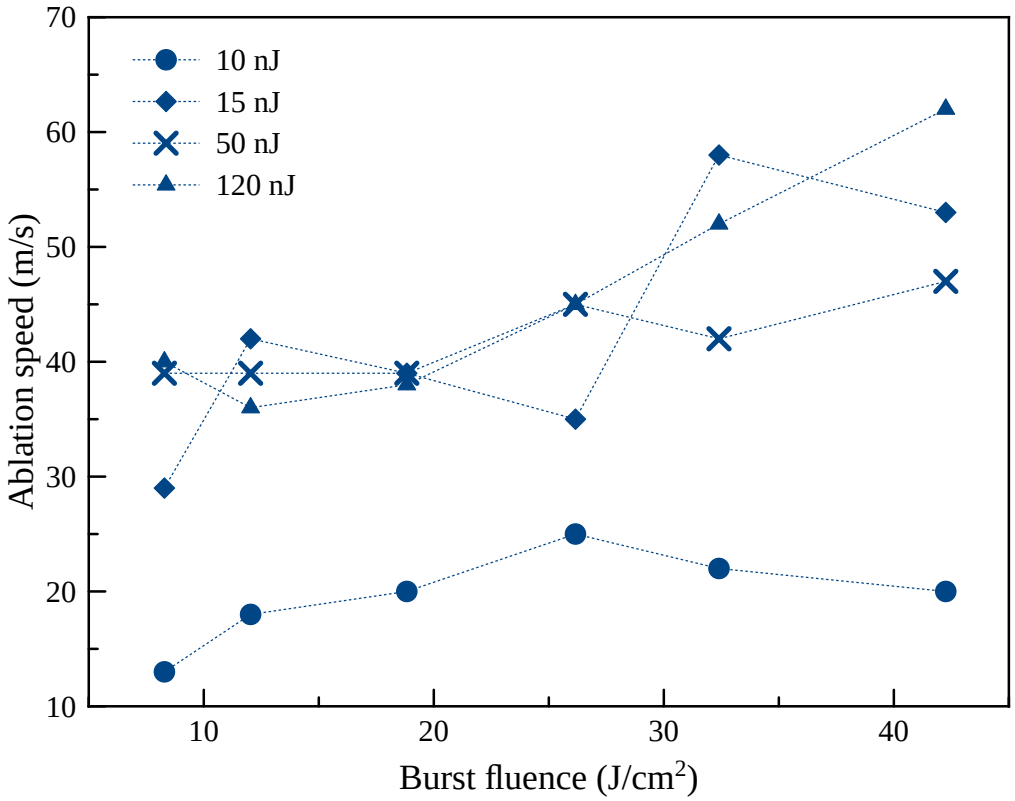

Figure 3.9: Ablation speed measurements for different pulse energies at 13 GHz repetition rate.

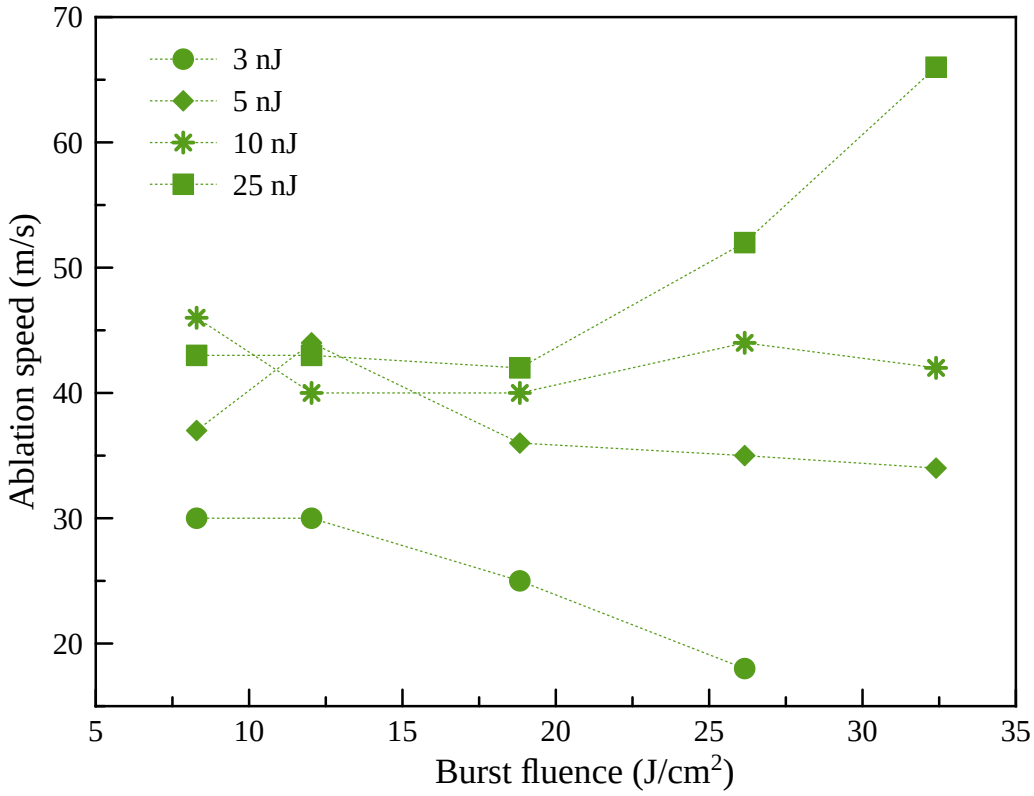

Figure 3.10: Ablation speed measurements for different pulse energies at 52 GHz repetition rate.

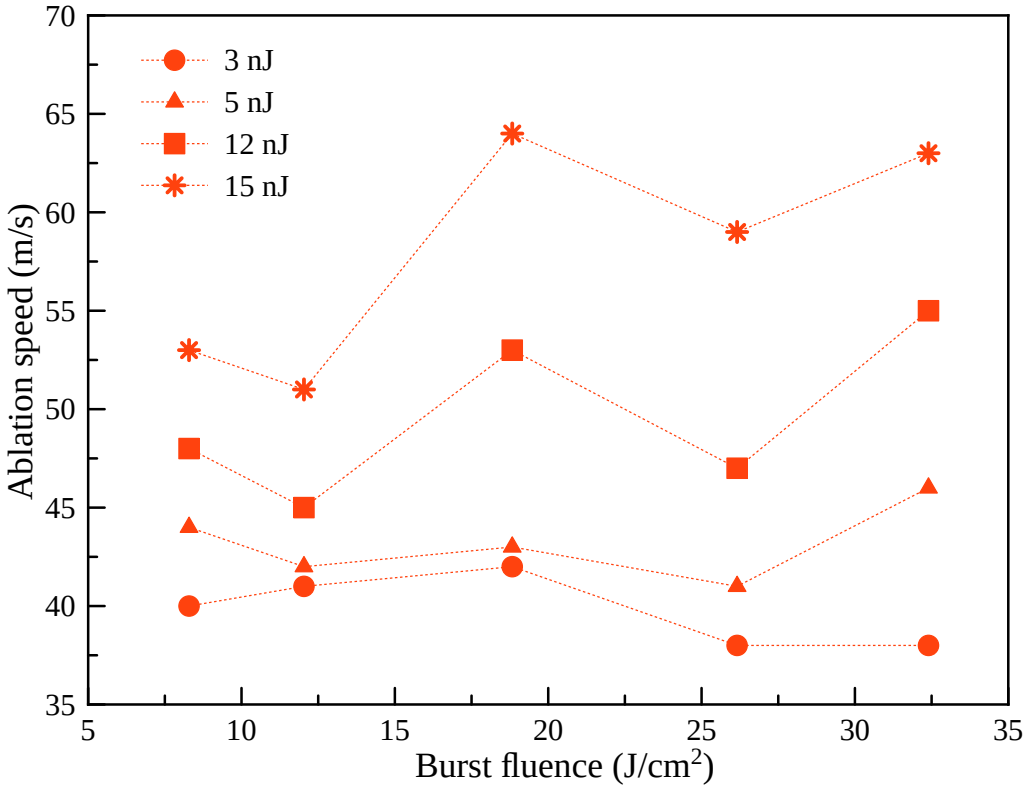

Figure 3.11: Ablation speed measurements for different pulse energies at 104 GHz repetition rate.

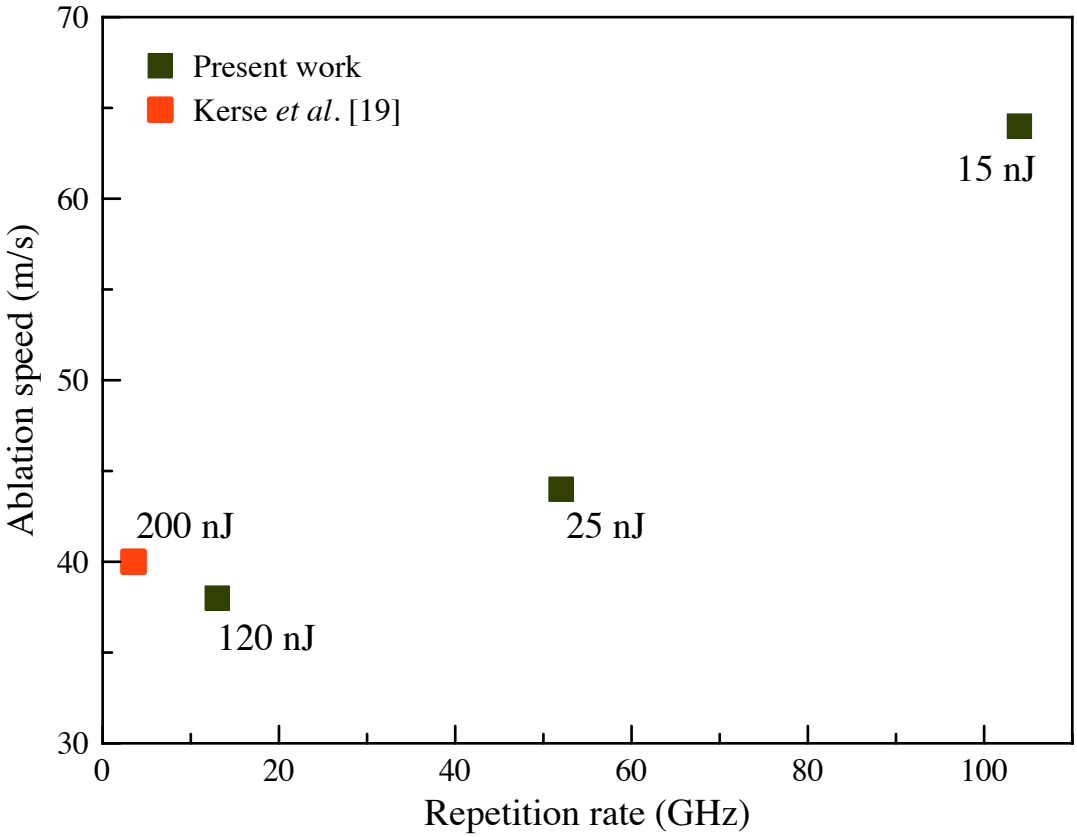

Figure 3.12: Ablation speed measurements for different pulse energies with increasing GHz repetition rate.

After exploring ablation speeds at these three repetition rates, we can now perceive the bigger picture. With increasing repetition rates, we can achieve very high ablation speeds at much lower fluences. It is also clear that an optimal regime exists in terms of the burst fluence to obtain the highest ablation speed for a given repetition rate.

The plot in figure 3.12 compares the highest ablation speed obtained in the present study at different pulse repletion rates for the same burst fluence of 19 J/cm^2. On the same plot, we can see what the state of the art [19] is for linear ablation speed. The key difference here is that the highest speed obtained in [19] required two times higher burst fluence, and much higher pulse energy, which agrees with our observation that higher repetition rates can significantly increase the ablation speed while scaling down the necessary pulse energy at any given burst fluence. All the experimental data shown in figures 3.9-3.12 were obtained with a spot size of $\sim 23\,\mu$m.

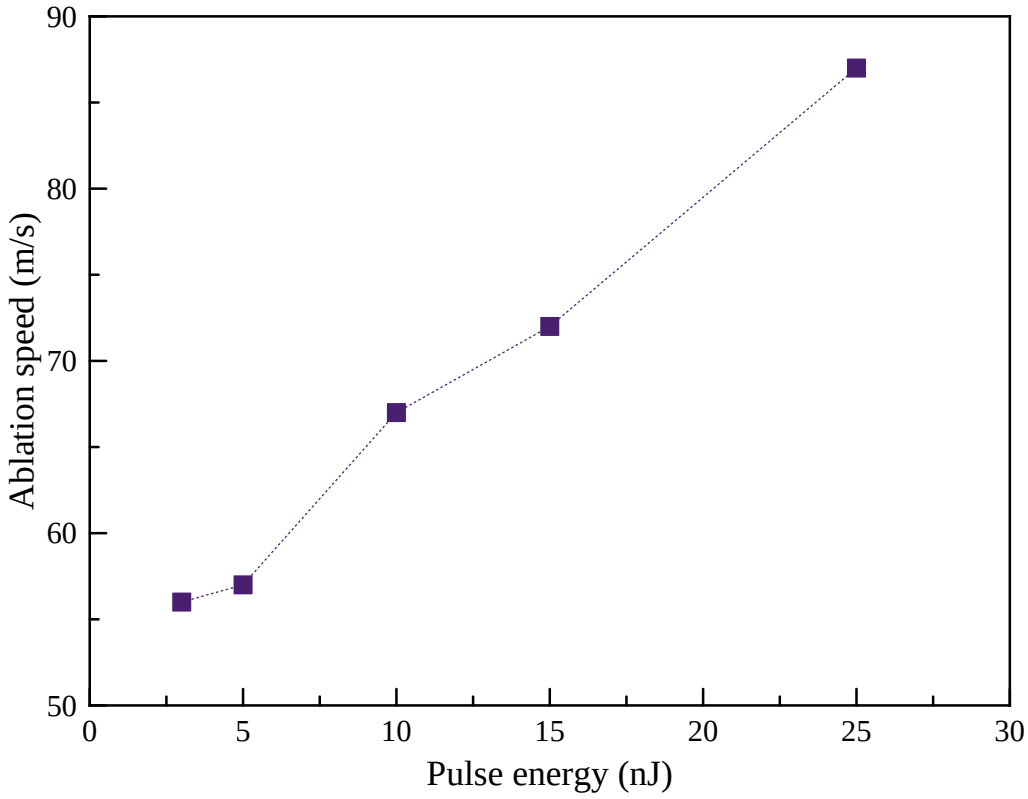

Figure 3.13: Ablation speed measurements with increasing pulse energies and constant burst fluence of 76 J/cm^2 at 52 GHz repetition rate using $\sim$ 10 µm spot size.

We did a set of experiments using 10$\times$ objective lens at a 52 GHz repetition rate with $\sim$ 10 µm spot size to observe the range of ablation speed at much higher fluence (figure 3.13). We changed the pulse energy and used a constant fluence of 76 J/cm^2. We found that a very high ablation speed of 87 m/s could be obtained using 25 nJ pulse energy, which is the same pulse energy that gave the highest ablation speed at 52 GHz in the experiments using a galvanometer scanner ($\sim$ 23 µm spot size).

Based on our observations, we predict that if we can maintain the high efficiency as we increase the pulse repetition rate and approach the THz regime, we expect to reach ablation speed orders of magnitude higher than the current result. As we already achieved 87 m/s speed of ablation at 52 GHz repetition rate, we would expect a 20$\times$ higher speed at 1 THz, which is 1.7 km/s. This implies that there might exist a new regime where the material would be removed much faster than the speed of

sound in air, showing an indication of approaching the speed of sound in silicon.

Chapter 4

Applications

We successfully applied our knowledge of silicon ablation at very high pulse repetition rates to a range of very different materials which have medical and industrial importance.

4.1 Thin Film Removal from Glass

The 52 GHz repetition rate laser was used to demonstrate the removal of thin film from a glass sample. This was an industrial-grade glass with a special conductive coating. Different sets of laser parameters, e.g., pulse energy, burst energy, and burst durations, were applied to see which parameters work better for this material. Table 4.1 shows the optical and scanning parameters used for this sample. The overlap between bursts was 90% in both x and y axes of scanning, as this degree of overlap gave very high surface quality after processing. Although the trade-off here was that, larger overlap requires relatively longer scanning time, but our main goal was to remove the coating entirely from the glass. If necessary, the scanning speed could be increased easily by increasing the burst repetition rates and simultaneously adjusting the scanning speed of the galvanometer scanner. But here we focused on the quality of ablation rather than the scanning time as this was a trivial matter. Figure 4.1 shows a glass sample

Figure 4.1: Coated glass sample. The writings and the shapes were drawn by ablating the coating with different laser parameters.

where we used different laser parameters to make different shapes and writings by removing the coating from the glass. The transparency of the shapes indicates that the coating was successfully removed using a pulse energy of 25 nJ. On the other hand, the writings show an orangish color, which was processed with 10 nJ pulses and the coating was not removed completely.

For more systematic experiments, we scanned over a 6 mm $\times$ 6 mm area on the sample with 6 different parameters shown in table 4.1. Three sets of experiments were done with 10 nJ pulses with three different numbers of scanning loops, and the other three were done in the same manner but with 25 nJ pulse energy. From figures 4.2 and 4.3, we can see that the quality of coating removal is better when we used 25 nJ/pulse instead of 10 nJ/pulse (leaves a thin orange layer, which could be due to heating instead of ablation). Even 1 pass of scanning using 25 nJ/pulse could bring similar results as that obtained using 10 nJ/pulse with 3 passes (comparing figures 4.2 (c) and 4.3 (a)). If we look at the figures 4.3 (b) and 4.3 (c), we cannot observe any significant difference between them. We infer that we can remove the coating with just two passes by using 25 nJ/pulse.

As the thin film was conductive, there was a more reliable way to check if the

Table 4.1: Laser parameters for thin film removal experiments.

No. of sets	Pulse energy (nJ)	Average power (W)	No. of passes	Processing time (s)
1	10	4.8	1	94
2	10	4.8	2	182
3	10	4.8	3	282
4	25	4.8	1	93
5	25	4.8	2	182
6	25	4.8	3	282

coating was removed completely. We used an ohm-meter and measured the resistance of the sample with two probes. First, we pressed both the probes at two points on the coating, and it gave nearly zero resistance. Then we put the probes at two points on the surface of the processed area, and it showed resistance of several hundreds of MΩ for the last two experiments (25 nJ/pulse, 4.8 W with 2 passes and 3 passes). This confirms that we were able to remove a significant amount of the conductive layers of the coating.

We also checked the transmission of light through these ablated surfaces by using a sensitive power meter under the sample. The highest transmission was found again from the last two experiments (25 nJ/pulse, 4.8 W with 2 passes and 3 passes), which was 95%. We then measured the transmission of a regular microscope slide, which was also 95%.

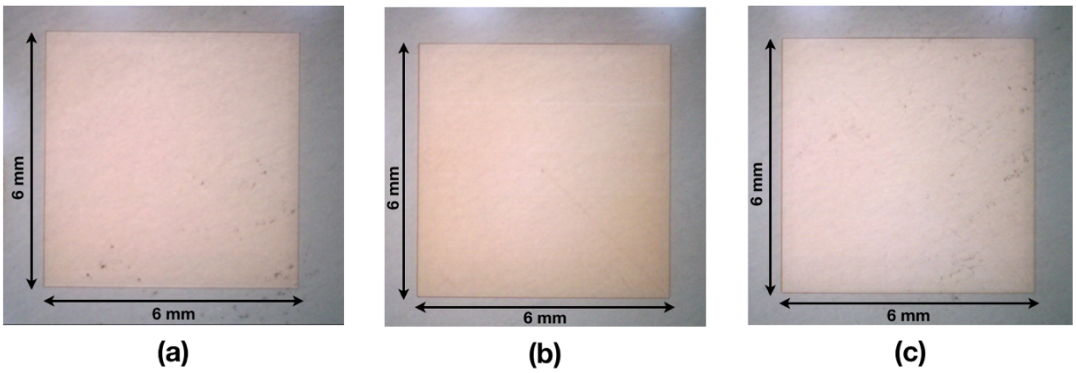

Figure 4.2: Light microscope image of processed areas using 10 nJ/pulse and 4.8 W average power (a) after 1 pass (b) after 2 passes, (c) after 3 passes.

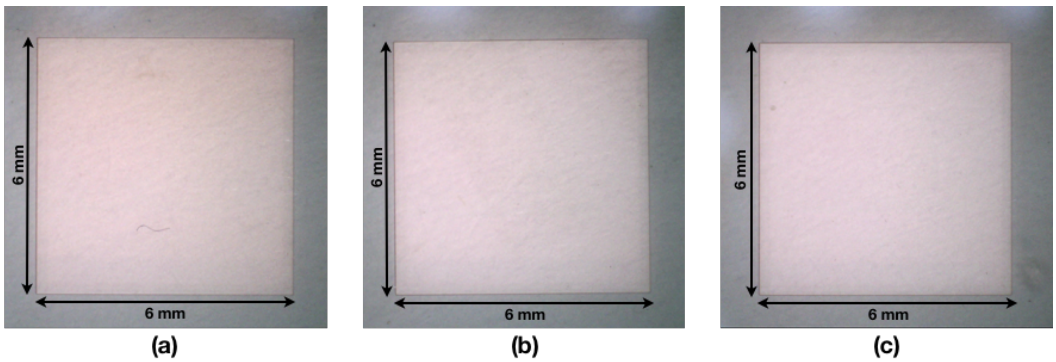

Figure 4.3: Light microscope image of processed areas using 25 nJ/pulse and 4.8 W average power (a) after 1 pass (b) after 2 passes, (c) after 3 passes.

Based on these preliminary experiments, we conclude that 25 nJ/pulse at 4.8 W with two passes over the sample was optimal in terms of processing speed and coating removal quality among the abovementioned six sets of experiments.

4.2 Cutting of Intraocular Lenses

Preliminary experiments were done with different pulse energies on intraocular lens samples. Intraocular lens samples need precise cutting as these are used in cataract surgery. In our initial investigations, we could achieve ablation on lens samples using 10 nJ and 25 nJ pulse energies. Lines were cut by scanning the laser back and forth with a different number of passes. The Pockels cell was used to gate the bursts at low repetition rates, and a 3D motorized stage was used to move the sample. For these experiments, 500 Hz frequency of the Pockels cell was used, so the average power dropped to a few tens of mJ.

With 25 nJ pulses and 80 µJ burst energy, 50 passes of scanning gave a cut of 10 µm depth (figure 4.4). We did another experiment using 10 nJ pulse energy and 80 µJ burst energy. This time we slowly increased the height of the sample by a few tens of micrometers while processing with 40 passes of scanning. This experiment gave a cut of 70 µm deep channel, as seen in figure 4.5.

From the results of silicon experiments, we already knew that for different materials at a particular repetition rate, certain laser parameters work more efficiently. For this intraocular lens material, 10 nJ worked better than 25 nJ.

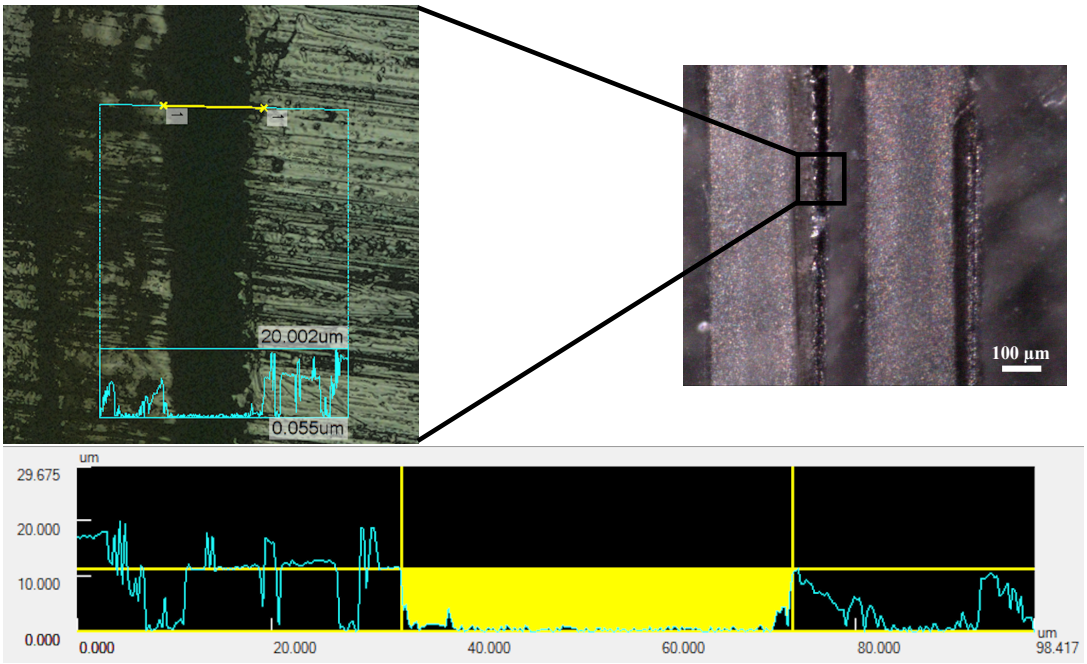

Figure 4.4: Experiment with 50 passes of scanning using 25 nJ pulse energy, 80 µJ burst energy and 40 mW average power.

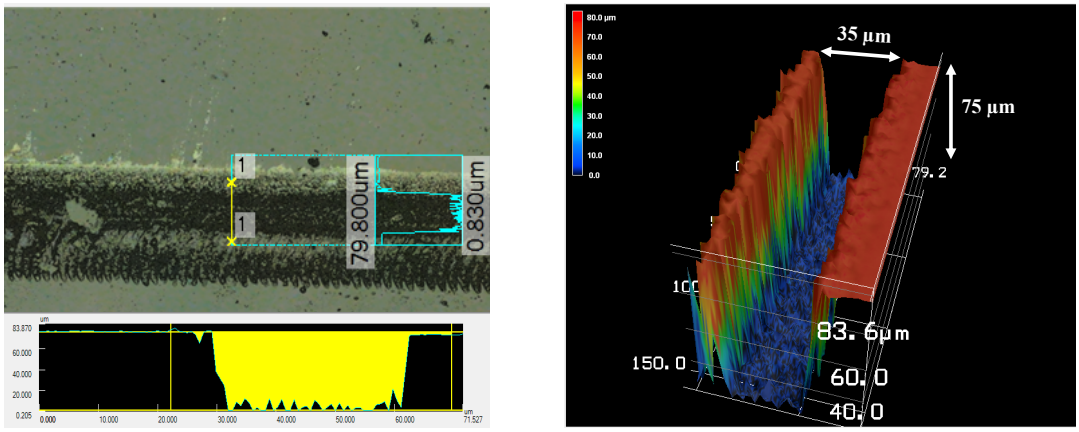

Figure 4.5: Experiment with 40 passes of scanning using 10 nJ pulse energy, 80 µJ burst energy and 40 mW average power.

Table 4.2: Laser parameters for preliminary experiments on intraocular lens.

No. of sets	Pulse energy (nJ)	Average power (mW)	No. of passes	Processing time (s)
1	10	40	40	29
2	25	40	50	36

4.3 Nitinol Processing

After finishing the silicon characterization at 104 GHz repetition rate, a material different from silicon available at that time was used to see how this laser works on other materials. The available material was nitinol, an alloy of nickel and titanium, where the atomic percentage of the two material is roughly the same. Nitinol is an important alloy with two unique properties, shape memory and super-elasticity. Shape memory can be defined as a property of a material that undergoes deformation at a particular temperature (transformation temperature) and remains in the deformed shape even when the external force is removed. If heat is applied to the material that raises the temperature above the transformation temperature, it can go back to its original shape. This property is referred to as shape memory. The other property called super-elasticity can be defined as the property of the material that can undergo large stress and can return to its original phase when the stress load is removed.

The 104 GHz repetition rate was used on a nitinol tube to make a 0.2 mm $\times$ 10 mm channel area. The preliminary testing of laser parameters on nitinol was done using 3 nJ, 5 nJ and 10 nJ pulse energies. Among the three pulse energies, 5 nJ turned out to be the most efficient one for this material. Table 4.3 shows the parameters that gave the best results.

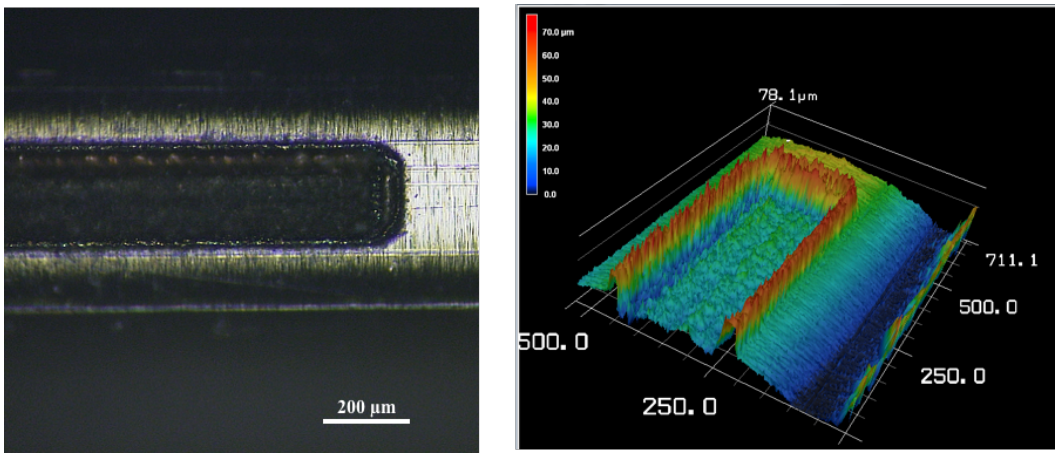

Figure 4.6: LSM image and 3D profile of the processed sample using 5 nJ/pulse, 4.8 W and 10 passes, showing the average depth of $\sim 23\,\mu m$.

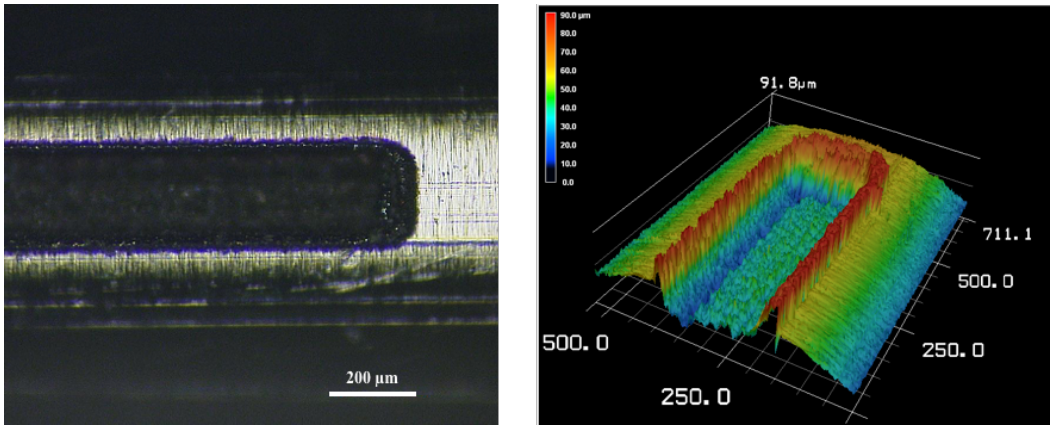

Figure 4.7: LSM image and 3D profile of the processed sample using 5 nJ/pulse, 4.8 W and 20 passes, showing the average depth of 38 µm.

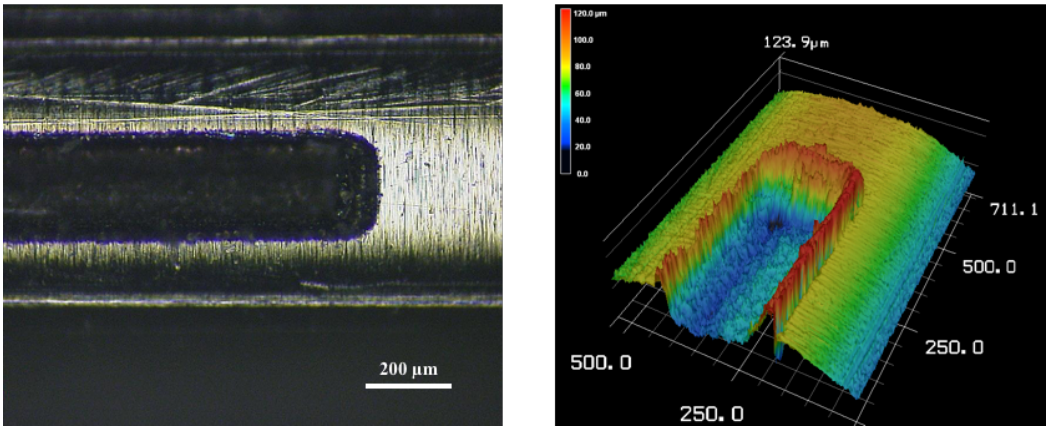

Figure 4.8: LSM image and 3D profile of the processed sample using 5 nJ/pulse, 4.8 W and 30 passes, showing the average depth of 60 µm.

Table 4.3: Laser parameters for preliminary experiments on nitinol.

No. of sets	Pulse energy (nJ)	No. of passes	Average power (W)	Processing time (s)
1	5	10	4.8	5.2
2	5	20	4.8	10.3
3	5	30	4.8	15.4

Chapter 5

Conclusion

In this thesis, the study of ablation cooled regime has been extended, which was first introduced in [19]. This study is also a continuation of part of the work done in [20] up to 13 GHz repetition rate. In the current work, ablation efficiency characteristics and another important parameter, namely, the ablation speed were explored at very high pulse repetition rates.

For all the experiments, custom-built, fiber-based master-oscillator power-amplifier systems have been used. These lasers were built with Yb-doped fibers, emitting laser output with central wavelength at 1030 nm. The high repetition rates up to 52 GHz were achieved by adding cascaded series of 50/50 couplers. After that, in order to avoid the difficulty of precision-cutting of fibers within a few millimeters of tolerance to implement RRM to achieve 104 GHz repetition rate, a free-space repetition rate multiplier was used. In order to achieve more control over the burst repetition rates for several experiments, the Pockels cell was introduced in the laser system.

For data collection and imaging, laser scanning microscopy and scanning electron microscopy have been used extensively. No post-processing of the sample was needed other than cleaning the sample with acetone using an ultrasonic cleaner to get rid of some nano-micro particles generated during the ablation process. For the characterization of the ablated craters, LSM and SEM measurements were taken, and

depth, diameter, and volume information were collected. From these data, ablation efficiency and ablation speed were calculated.

From previous [19] and current work, we can understand the ablation cooled regime's general feature, which is, when the pulse repetition rate is increased, the ablation efficiency drops at higher pulse energies due to the plasma shielding effect. The onset of this regime starts at different pulse repetition rates for different materials. For silicon, it begins at some point between 27 MHz and 108 MHz as a jump in the ablation efficiency is observed [19]. If the repetition rate increases without proper scaling of the pulse energy, a drop in the ablated volume and, therefore, a lower value of ablation efficiency is observed. This drop occurs due to the expected plasma shielding effect. As we explored deep inside the ablation cooled regime at around 30 times higher repetition rate than the state of the art [19], the pulse energy for efficient ablation was lowered by a factor of $\sim$50. Therefore, ablation could be achieved at very low pulse energies, which could potentially be obtained directly from mode-locked lasers, effectively making the expensive and complicated designs of laser amplifiers redundant.

The experimental data showed that at higher repetition rates, the most efficient pulse energy for ablation becomes a few nano joules. For 104 GHz and 52 GHz, the best ablation efficiency was obtained at 3 nJ, and 5 nJ pulse energies, whereas for 13 GHz, the most efficient pulse energy was 15 and 25 nJ. So, the pulse energy for ablation has been reduced significantly from the state of the art, which was a few hundreds of nano Joules [19]. Another interesting feature was observed as we moved to higher repetition rate experiments. As the repetition rate was increased up to 100 GHz, the efficiency started to drop. At 13 GHz, the highest efficiency was recorded to be 2.5 mm^3/Wmin. At 52 GHz, it was 1.9 mm^3/Wmin, and at 104 GHz, it was 1.7 mm^3/Wmin. The reduction in ablation efficiency at higher repetition rates is indeed an expected outcome due to its dependence on pulse duration. In all the experiments, the repetition rates were increased significantly, but the pulse duration was set at $\sim$1 ps for all three repetition rates. For a semiconductor like silicon, the nonlinear absorption could be dominated by two-photon absorption. Thus, the ablation efficiency would be a quadratic function of the repetition rate. If the pulse duration is kept constant, the ablation efficiency would reach the highest value at a specific repetition rate

and then start dropping as we increase the repetition rate. This is what we observed in this experimental study.

Among the three repetition rates explored here, the highest ablation speed was obtained at 104 GHz repetition rate at a particular burst fluence. The tradeoff here is that with increasing repetition rates, the ablation speed could be escalated significantly at very low pulse energies, but at the same time, the ablation efficiency drops. At 104 GHz repetition rate, the highest speed of ablation observed was 64 m/s using 15 nJ pulse energy. At the same laser fluence at 13 GHz, the ablation speed was two times lower, but much higher pulse energy was needed, which was 120 nJ. So, among the three repetition rates explored, with 8 times higher repetition rates, we could achieve two times higher ablation speed at 8 times lower pulse energy. A more extensive experimental study focused on this area could open the door for a new paradigm on ablation cooled material processing with much higher ablation speed. The results obtained in this study show a clear indication of a very high-speed ablation regime at even higher repetition rates. The drop in efficiency at higher repetition rates could be compensated by decreasing the pulse duration by the same factor by which the repetition rate would increase. This way, the number of sacrificial pulses could be reduced, and a smaller number of pulses would be needed to ablate the same amount of material at much higher speeds. To further increase the ablation speed than what has already been achieved here, a femtosecond laser would be needed as the current work is based on 1 ps systems. For example, the highest efficiency we could obtain in our experiments was at 13 GHz repetition rate. We predict that, in order to maintain that effeciency at even higher repetition rate, e.g., at 104 GHz (8 times higher), we need to decrease the pulse duration by a factor of 8. Which means, we need a laser system with 125 fs pulses at 104 GHz repetition rate to avoid the drop in efficiency.

The experimental study of ablation speed in the present work would contribute significantly to this area of research as it indicates the possibility of very high-speed material processing. A more detailed study of this high-speed ablation regime is necessary to understand the mechanism fully. This research could be applied to process industrially relevant materials for high-speed micromachining. But most importantly, we are now one step closer to a long-term goal, which is live tissue surgery. From

literature, it is a known fact that lasers are extremely capable tools, but they lag behind applications in medical surgery due to their processing speeds. Although lasers are being used for some medical purposes, for example, in cataract eye surgery or removing skin hyperpigmentation, the real ability of lasers is yet to be explored in the surgical fields where the processing time is currently the most limiting factor.

Bibliography

[1] T. H. Maiman, "Stimulated optical radiation in ruby," *Nature*, vol. 187, no. 4736, p. 493, 1960.

[2] A. Javan, W. R. Bennett Jr, and D. R. Herriott, "Population inversion and continuous optical maser oscillation in a gas discharge containing a He-Ne mixture," *Physical Review Letters*, vol. 6, no. 3, p. 106, 1961.

[3] C. K. N. Patel, "Continuous-wave laser action on vibrational-rotational transitions of CO_2," *Physical Review*, vol. 136, no. 5A, p. A1187, 1964.

[4] P. A. Hilton, "Early days of laser cutting," in *Lasers in Material Processing*, vol. 3097, p. 10, International Society for Optics and Photonics, 1997.

[5] M. M. Zaret *et al.*, "Ocular lesions produced by an optical maser (laser)," *Science*, vol. 134, no. 3489, p. 1525, 1961.

[6] L. Goldman *et al.*, "Effect of the laser beam on the skin," *Journal of Investigative Dermatology*, vol. 40, no. 121, p. 2, 1963.

[7] R. C. J. Verschueren, "Technical problems of carbon dioxide laser surgery in the rectum," *The Biomedical Laser: Technology and Clinical Applications*. New York, NY: Springer New York, 1981.

[8] C. R. Youmans *et al.*, "Cystoscopic control of gastric hemorrhage," *Archives of Surgery*, vol. 100, no. 6, p. 721, 1970.

[9] G. Nath, W. Gorisch, and P. Kiefhaber, "First laser endoscopy via a fiberoptic transmission system," *Endoscopy*, vol. 5, no. 04, p. 208, 1973.

[10] P. Kiefhaber, G. Nath, and K. Moritz, "Endoscopical control of massive gastrointestinal hemorrhage by irradiation with a high-power Neodymium-Yag laser," *Progress in Surgery*, vol. 15, p. 140, 1977.

[11] L. Toty *et al.*, "Bronchoscopic management of tracheal lesions using the neodynium yttrium aluminium garnet laser," *Thorax*, vol. 36, no. 3, p. 175, 1981.

[12] D. Fleischer, F. Kessler, and O. Haye, "Endoscopic Nd:YAG laser therapy for carcinoma of the esophagus: a new palliative approach," *The American Journal of Surgery*, vol. 143, no. 3, p. 280, 1982.

[13] T. Juhasz *et al.*, "Corneal refractive surgery with femtosecond lasers," *IEEE Journal of Selected Topics in Quantum Electronics*, vol. 5, no. 4, p. 902, 1999.

[14] N. Mamalis, "Femtosecond laser: the future of cataract surgery?," *Journal of Cataract & Refractive Surgery*, vol. 37, no. 7, p. 1177, 2011.

[15] P. S. Binder, "Flap dimensions created with the intralase fs laser," *Journal of Cataract & Refractive Surgery*, vol. 30, no. 1, p. 26, 2004.

[16] P. Pronko *et al.*, "Machining of sub-micron holes using a femtosecond laser at 800 nm," *Optics Communications*, vol. 114, no. 1, p. 106, 1995.

[17] A. DeMaria, D. Stetser, and H. Heynau, "Self mode-locking of lasers with saturable absorbers," *Applied Physics Letters*, vol. 8, no. 7, p. 174, 1966.

[18] U. Keller *et al.*, "Solid-state low-loss intracavity saturable absorber for Nd: YLF lasers: an antiresonant semiconductor Fabry–Perot saturable absorber," *Optics Letters*, vol. 17, no. 7, p. 505, 1992.

[19] U. Keller, "Recent developments in compact ultrafast lasers," *Nature*, vol. 424, no. 6950, p. 831, 2003.

[20] C. Kerse *et al.*, "Ablation-cooled material removal with ultrafast bursts of pulses," *Nature*, vol. 537, no. 7618, p. 84, 2016.

[21] D. K. Kesim, "Tailoring nonlinear temperature profile in laser-material processing," PhD thesis, Bilkent University, 2019.

[22] D. Sands, "Pulsed laser heating and melting," *Heat Transfer-Engineering Applications*, p. 47, 2011.

[23] W. M. Rohsenow *et al.*, *Handbook of Heat Transfer*, vol. 3. McGraw-Hill New York, 1998.

[24] M. Knowles *et al.*, "Micro-machining of metals, ceramics and polymers using nanosecond lasers," *The International Journal of Advanced Manufacturing Technology*, vol. 33, no. 1, p. 95, 2007.

[25] D. F. Swinehart, "The Beer-Lambert law," *Journal of Chemical Education*, vol. 39, no. 7, p. 333, 1962.

[26] A. Turnalı, "Three dimensional processing of silicon with pulsed lasers for optical applications," MS thesis, Bilkent University, 2015.

[27] D. Strickland and G. Mourou, "Compression of amplified chirped optical pulses," *Optics Communications*, vol. 56, no. 3, p. 219, 1985.

[28] A. Sugar, "Ultrafast (femtosecond) laser refractive surgery," *Current Opinion in Ophthalmology*, vol. 13, no. 4, p. 246, 2002.

[29] R. S. Marjoribanks *et al.*, "Ablation and thermal effects in treatment of hard and soft materials and biotissues using ultrafast-laser pulse-train bursts," *Photonics & Lasers in Medicine*, vol. 1, no. 3, p. 155, 2012.

[30] M. Lapczyna *et al.*, "Ultra high repetition rate (133 MHz) laser ablation of aluminum with 1.2-ps pulses," *Applied Physics A*, vol. 69, no. 1, p. S883, 1999.

[31] M. A. Green and M. J. Keevers, "Optical properties of intrinsic silicon at 300 K," *Progress in Photovoltaics: Research and Applications*, vol. 3, no. 3, p. 189, 1995.

[32] J. Petelin *et al.*, "Burst shaping in a fiber-amplifier chain seeded by a gain-switched laser diode," *Applied Optics*, vol. 54, no. 15, p. 4629, 2015.